FACULTY
OF MATHEMATICS
AND PHYSICS
Charles University

MASTER THESIS

Anna Terynková

Metastable alloy Ti-15Mo prepared by powder metallurgy

Department of Physics of Materials

Supervisor of the master thesis: RNDr. Kristína Bartha

Study programme: Physics

Specialization: Physics of Condensed Matter and Materials

Prague 2019

I declare that I carried out this master thesis independently, and only with the cited sources, literature and other professional sources.

I understand that my work relates to the rights and obligations under the Act No. 121/2000 Coll., the Copyright Act, as amended, in particular the fact that the Charles University has the right to conclude a license agreement on the use of this work as a school work pursuant to Section 60 paragraph 1 of the Copyright Act.

In…..... date.....

Acknowledgement

I would like to express my gratitude to my supervisor RNDr. Kristína Bartha for factual comments to my master thesis and for being available whenever I needed. I would also like to thank RNDr. Josef Stráský, Ph.D. who helped me interpret the results of my research and was very patient whenever I needed help. My gratitude belongs also to Prof. RNDr. Miloš Janeček, PhD. who was available literally day and night. Last but not least, I would like to thank RNDr. Petr Harcuba, Ph.D. and Mgr. Jiří Kozlík for their assistance.

Title: Metastable alloy Ti-15Mo prepared by powder metallurgy

Author: Anna Terynková

Department / Institute: Department of Physics of Materials

Supervisor of the master thesis: RNDr. Kristína Bartha, Department of Physics of Materials

Abstract: This diploma thesis focused on manufacturing and characterization of Ti-15Mo metastable beta-Ti alloy prepared by cryogenic milling and spark plasma sintering. Initial powder was prepared by gas atomization and consequently deformed by cryogenic milling (milled powder). Both initial and milled powders were compacted by spark plasma sintering (SPS) at temperatures from 750 °C to 850 °C. Dependence of microstructure and mechanical properties on the parameters of preparation was studied.

During cryo-milling, powder particles significantly changed shape from ball-shaped to disc-shaped. Particles were not refined by milling, but severely plastically deformed. SEM observations showed that all prepared samples contain duplex alpha + beta structure. Volume fraction of alpha phase is significantly higher in the sintered milled powder due to increased beta-transus temperature caused by contamination by oxygen and also due to easier alpha phase precipitation caused by refined microstructure.

Maximum microhardness of 350 HV was achieved for both types of sintered powders. High microhardness of sintered initial powder can be attributed to formation of omega phase during cooling, while sintered milled powder is strengthened by refined microstructure and small alpha phase precipitates.

Cryogenic milling prior to sintering allows achieving fully dense compact material with high microhardness at comparatively lower sintering temperatures.

Keywords: metastable β-titanium alloys, powder metallurgy, cryogenic milling, spark plasma sintering

Contents

Introduction 1

1 Theoretical background 2

1.1 Titanium and its alloys 2

1.1.1 Titanium 2

1.1.2 Classification of alloying elements 3

1.1.3 Metastable phases 4

1.1.4 Classification of titanium alloys 5

1.1.5 Phase transformations 6

1.1.6 Metastable β-Ti alloys 8

1.1.7 Ti-15Mo alloy 8

1.2 Ultrafine grained materials 9

1.2.1 Ultra-fine grained β-alloys 10

1.3 Recovery, recrystallization and grain growth 11

2 Powder metallurgy 13

2.1 Mechanical milling 13

2.2 Spark plasma sintering 14

2.3 Milling and sintering of Ti alloys – literature review 16

3 Aims of the thesis 18

4 Experimental material and characterization methods 19

4.1 Material preparation 19

4.1.1 Cryogenic milling 19

4.1.2 Spark plasma sintering 20

4.2 Sample preparation 21

4.3 Scanning electron microscopy 22

4.3.1 Electron back-scattered diffraction 24

4.3.2 Transmission Kikuchi diffraction 27
4.3.3 Focused ion beam 28
4.4 X-ray diffraction 29
4.5 Carrier gas hot extraction 30
4.6 Mechanical properties measurement 30
4.6.1 Microhardness measurements 30
4.6.2 Deformation tests 31
5 Results 34
5.1 Powders 34
5.1.1 Microstructure observed by a SEM 34
5.1.2 Chemical contamination measured by CGHE 35
5.2 Bulk sintered material 35
5.2.1 Microstructure of sintered initial powder 35
5.2.2 Microstructure of sintered milled powders 43
5.2.3 Phase composition measured by XRD 48
5.2.4 Chemical contamination measured by CGHE 50
5.2.5 Mechanical properties 51
6 Discussion 54
6.1 Cryogenic milling 54
6.2 Spark plasma sintering of initial and milled powder 54
6.2.1 Compaction 54
6.2.2 Phase composition 55
6.2.3 Mechanical properties 57
Conclusions 60
Bibliography 61

Introduction

Titanium and its alloys are suitable for utilization in many branches of industrial production due to their unique properties: excellent corrosion resistance, low density in comparison with steels and Ni-based superalloys, good specific strength and sufficient biocompatibility. Nowadays, they are used especially in aircraft industry but they are perspective for utilization also in medicine, architecture, marine or offshore [1]. Drawbacks in industrial applications are their high costs due to difficult process of preparation. Metastable β-titanium alloys are the most investigated class of titanium alloys nowadays due to their promising properties such as high strength.

Powder metallurgy (PM) is an alternative way of production titanium alloys as it may reduce production costs due to near-net-shape processing. Bulk material is prepared by so-called bottom-top approach – compaction of powder of a given alloy.

It this diploma thesis, a powder of metastable β-titanium alloys Ti-15Mo was deformed by cryogenic milling and initial powder as well as milled powder were compacted by spark plasma sintering (SPS). The effects of cryogenic milling and parameters of sintering on microstructure and mechanical properties were investigated. Microstructure was studied by scanning electron microscopy (SEM) including electron backscatter diffraction (EBSD) and mechanical properties were investigated by microhardness measurements and deformation tests.

1 Theoretical background

1.1 Titanium and its alloys

1.1.1 Titanium

Titanium was discovered in the year 1791 by British mineralogist and chemist W. George who was investigating magnetic sand. By magnet he separated black mineral today known as ilmenite ($FeTiO_3$). By dissolving it in hydrochloric acid he got impure oxide (TiO_2) of a new element. A few years later, in 1795 a Berlin chemist M. H. Klaproth independently isolated the same TiO_2 oxide from an ore known as rutile and named the new element after children of Greek gods – Titans – from Greek mythology who were captured in Earth crust which is as hard as the extracting the ore [2]. Pure element was isolated more than a hundred years later in 1910 by M. A. Hunter.

Titanium has got the proton number of 22 and belongs to the 4^{th} period of periodic table of elements. Its density is 4.5 g/cm^3. The Earth's crust contains 0.6 % of titanium what makes it the fourth most abundant metal. In nature it occurs in a mixture of five isotopes of which ^{48}Ti is the most abundant (73.8 %). However, its commercial production has not started until 20^{th} century due to difficult and expensive process of isolation – Kroll's process – called after its Luxembourgish inventor G. Kroll. It is described by the following equations [2]:

$$TiO_2 + 2Cl_2 + 2C \rightarrow TiCl_4 + 2CO, \quad (1.1)$$

$$TiCl_4 + 2Mg \rightarrow 2MgCl_2 + Ti. \quad (1.2)$$

Titanium prepared by this process is referred to as "titanium sponge" because of its sponge-like appearance. In order to prepare bulk material, it must be crushed and melted in an inert atmosphere due titanium high reactivity with oxygen.

Titanium is a polymorphic material. It means it occurs in several crystallographic phases. At room temperature it crystallizes in a stable hexagonal close packed (HCP) α-phase. The unit cell of this phase is shown in Figure 1.1. Above the temperature of β-transus (882°C [2]) it transforms into the body-centred cubic (BCC) β-phase (Figure 1.2).

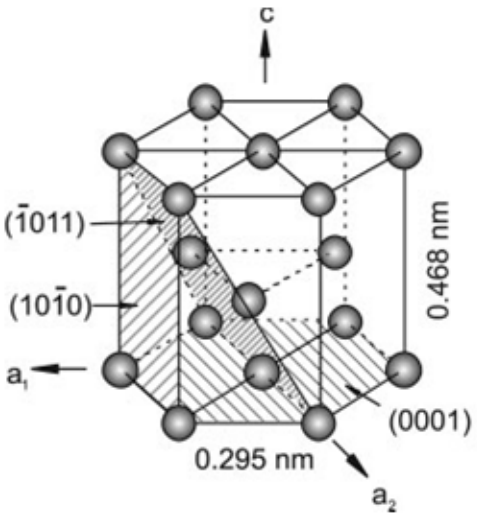

Figure 1.1: Hexagonal close-packed phase of α-phase [2]

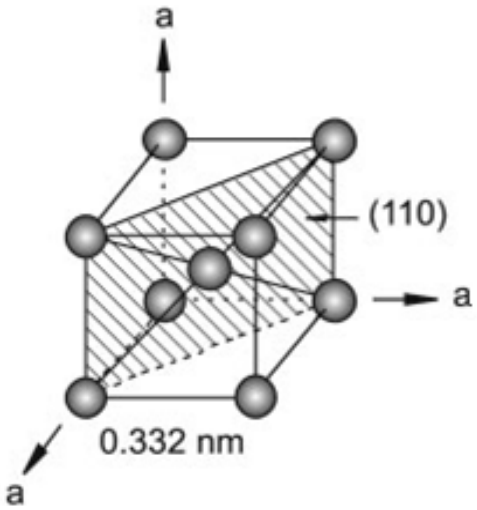

Figure 1.2: Body-centred cubic phase of β-phase [2]

1.1.2 Classification of alloying elements

Figure 1.3 shows the effect of different types of alloying elements in schematic phase diagrams. The alloying elements are divided by their effect on the temperature of β-transus into three groups:

- Neutral elements (e.g. Sn, Zr)
- α-stabilizing elements (e.g. Al, O, N, C)
- β-stabilizing elements (e.g. Mo, V, Ta, Nb)

Neutral elements have only minor influence on the temperature of β-transus while α-stabilizing elements increase it and extend the region of α-phase stability. On the other hand, β-stabilizing elements decrease the temperature of β-transus and extend the region of β-phase stability. β-stabilizing elements can be further divided into β-isomorphous elements and β-eutectoid forming elements. An alloy with sufficient amount of β-isomorphous elements contains the stable β-phase at room temperature while β-eutectoid forming elements are not completely soluble in titanium and adding only a low volume fraction of them may cause forming of intermetallic compounds.

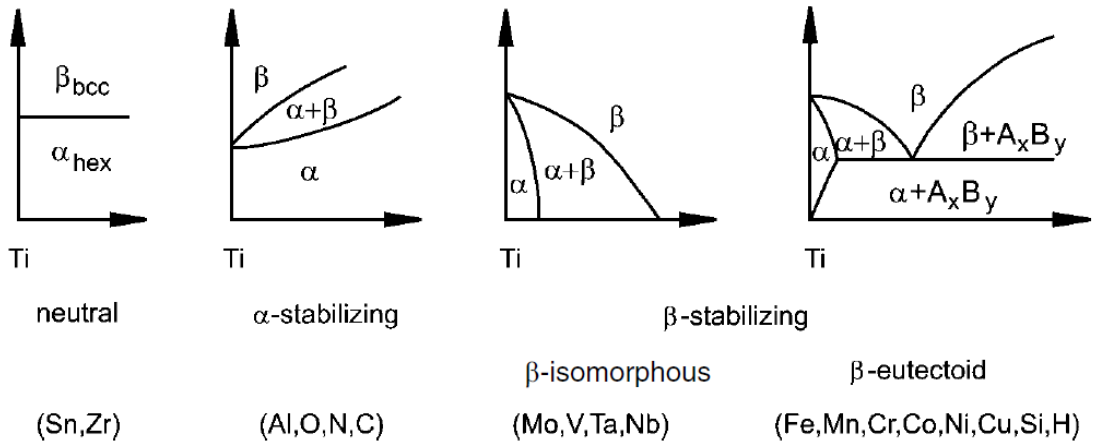

Figure 1.3: Effect of different type of alloying elements of a phase diagram of titanium alloys [1]

Equation (1.3) presents so-called Molybdenum equivalency. Molybdenum is a β-stabilizing element and as such it decreases the temperature of β-transus. β-stabilizing elements also prevent the formation of martensitic phases and 10 wt% of molybdenum is sufficient to suppress the martensite start temperature (M_s) marked by a dashed curve in Figure 1.4 below room temperature. Molybdenum equivalency (1.3) quantifies the effect of different elements on the temperature M_s by comparing them to molybdenum. For example, vanadium has only 2/3 of effect on M_s temperature (in wt%) in comparison with molybdenum. It means that adding 15 wt% into titanium is necessary for suppression the martensitic α-transformation below room temperature. Note that the minus sign for Al means that aluminium increases the M_s temperature as it is an α-stabilizing element.

$$[\mathrm{Mo}]_{\mathrm{eq.}} = [\mathrm{Mo}] + 0.67[\mathrm{V}] + 0.44[\mathrm{W}] + 0.28[\mathrm{Nb}] + 0.22[\mathrm{Ta}] \\ +2.9[\mathrm{Fe}] + 1.6[\mathrm{Cr}] + 1.25[\mathrm{Ni}] + 1.7[\mathrm{Mn}] + 1.7[\mathrm{Co}] - 1.0[\mathrm{Al}] \tag{1.3}$$

1.1.3 Metastable phases

Under given thermodynamic conditions (temperature, pressure), crystalline phases are either stable or metastable. Equilibrium (stable) phases occur in global minimum of Gibbs free energy G. Different configurations corresponding to local but not global minimum of G may be also present. These phases are non-equilibrium and are called metastable.

Besides above mentioned α and β-phases, titanium alloys may contain also some metastable ones. One of them is metastable martensite α' or α''. α' has the HCP structure while α'' is orthorhombic. α' and α'' form when the temperature decreases below the temperature M_S.

Hexagonal ω-phase is important for this thesis. ω-phase is formed by collapse of two neighbour planes $\{111\}_\beta$, while each third plane remains fixed [3, 4]. The β-phase plane (111) corresponds to the ω-phase plane (0001). ω-phase precipitates are coherent with the parent β-matrix. Two types of ω-phase according to mechanism of forming can be distinguished [5]. ω_{ath} (athermal) is formed during rapid quenching. Slightly bigger ω_{iso} (isothermal) particles are formed during annealing at temperatures 100-460 °C (the temperature range depends on the content of alloying elements). These two types of ω-phase are not completely independent, ω_{iso} usually transforms from ω_{ath} [6]. ω-phase can be also formed during deformation. ω-phase particles can act as a nucleation site of stable α-phase particles [7].

In alloys with higher amount of β-stabilizing elements a decomposition of β-phase to β_{rich} and β_{lean} phases occurs. These two phases differ in the amount of stabilizing elements and in lattice parameters.

1.1.4 Classification of titanium alloys

Titanium alloys can be divided into four groups, as shown in Figure 1.4: α-titanium alloys, α+β-titanium alloys, metastable β-titanium alloys and stable β-titanium alloys. α-alloys contain at room temperature only the α-phase. In these alloys mainly α-stabilizing or neutral alloying elements are present.

Alloys with appropriate amount of β-stabilizing elements which have the temperature of martensite start M_S above room temperature are called α+β-alloys. Martensitic phases α'/α'' form during quenching in these alloys. Ti-6Al-4V or Ti-6Al-7Nb alloys are examples of α+β-alloys.

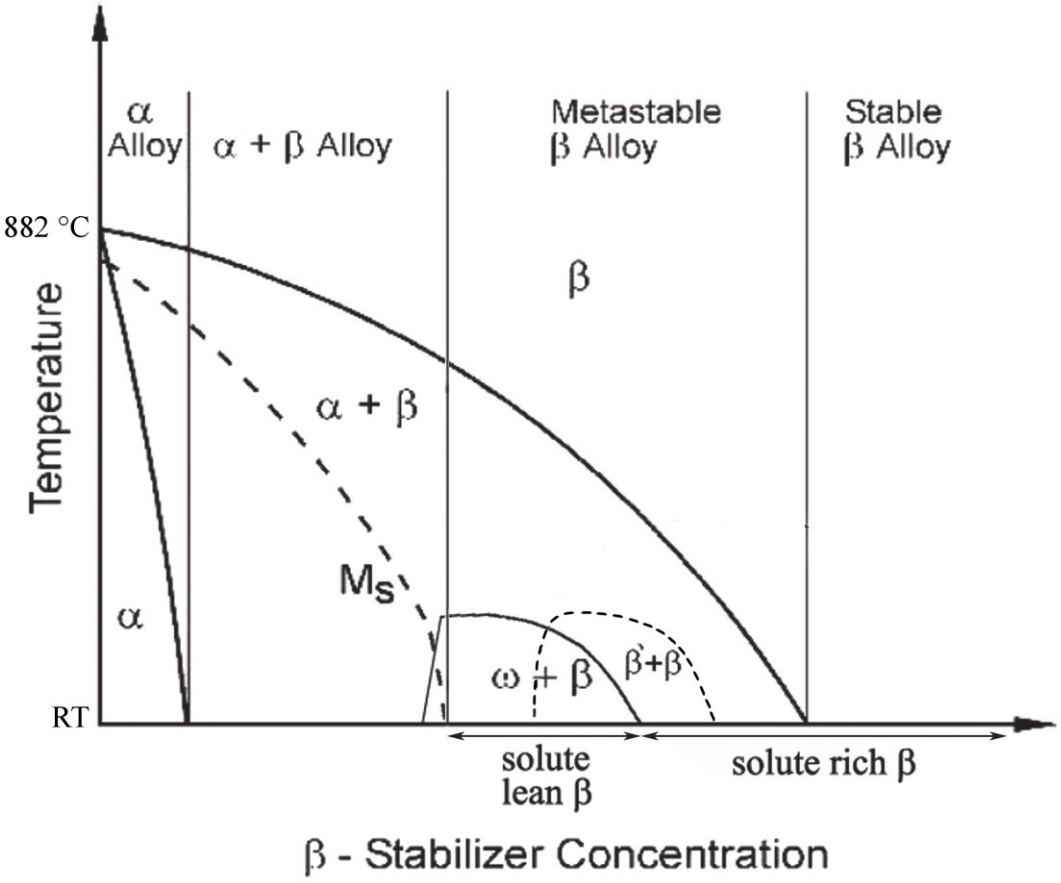

Figure 1.4: Pseudo-binary section of a β-isomorphous phase diagram [8]

Alloys with the content of β-stabilizing elements sufficiently high to suppress the temperature of martensite start below room temperature are called β-alloys. Metastable β-alloys are a less stabilized group of β-alloys. They do not contain martensitic phases when quenched from the temperature above the temperature of β-transus, however this state is metastable. In equilibrium, metastable β-alloys contain α+β-structure.

β-phase in alloys with sufficient content of β-stabilizing elements remains stable at room temperature – these alloys are called stable β-alloys.

The occurrence of metastable ω-phase and β_{rich} and β_{lean} phases is also noted in Figure 1.4.

1.1.5 Phase transformations

Two main mechanisms of phase transformations are diffusional phase transformations and martensitic phase transformations. During a diffusional

transformation, atoms migrate by vacancy mechanism and form a new structure. This type of transformation is thermally activated and irreversible. Chemical composition of emerging phases is often different from the parent phase (element partitioning). On the other hand, during a martensitic transformation, atoms move collectively at once for a short distance. The chemical composition is not changed and the transformation is reversible. In metastable β-titanium alloys, the most important transformations are β → α, β → ω and ω → α.

β → ω transformation:

Two types of ω-phase occur in metastable β-titanium alloys as mentioned above. ω_{ath} forms during quenching by a displacive transformation, while ω_{iso} forms during annealing by diffusional transformation. β-stabilizing elements diffuse from a growing ω_{iso}-particle into the parent β-matrix. The orientation relationship between ω-particle and β-matrix is the following:

$$(111)_\beta \parallel (00.1)_\omega \text{ and } [011]_\beta \parallel [11.0]_\omega \qquad (1.4)$$

As there are four sets of $\{111\}_\beta$ planes, four families of ω-phase may form. A model explaining ω-phase formation was described in [3, 9].

β → α transformation:

Transformation of α-phase from initial β-matrix is diffusional and takes place by nucleation and growth. There are several types of nucleation sites such as grain boundaries, α'/α'' martensitic phases, ω-particles or dislocations in deformed material [10, 11]. The shape and the size of α-particles depends on the temperature and time of annealing. Increasing temperature enhances the diffusion; however, the driving force for precipitation rapidly decreases as the temperature approaches the temperature of β-transus. Fine homogenously distributed α-phase particles can be formed by annealing below 450 °C by nucleation at ω-phase particles (so-called ω-assisted nucleation – as described below) [11]. Annealing above the temperature of 650 °C results in the inhomogeneous growth of α-phase particles at grain boundaries [12].

ω → α transformation:

The ω-assisted nucleation of the α-phase has previously been reported [7, 11, 13, 14]. It obeys the Burgers orientation relations for α-phase precipitating on β/ω interface:

$$(00.1)_\omega \parallel (\bar{1}2.0)_\alpha \parallel (\bar{1}11)_\beta$$
$$(\bar{1}\bar{1}.0)_\omega \parallel (00.1)_\alpha \parallel (0\bar{1}1)_\beta \quad (1.5)$$
$$[1\bar{1}.0]_\omega \parallel [10.1]_\alpha \parallel [211]_\beta$$

1.1.6 Metastable β-Ti alloys

Metastable β-titanium alloys are perspective for their high strength, excellent corrosion resistance and lower density in comparison with steels. Metastable β-titanium alloys such as Ti5553 (Ti-5Al-5V-5Mo-3Cr) are currently used in aircraft manufacturing (namely as landing gear structure) for their low specific density.

The utilization of metastable β-alloys in biomedicine is also expected. Nowadays, an α+β-alloy Ti-6Al-4V is used in orthopaedics. Vanadium is, however, considered as a toxic element. Although α+β-alloy Ti-6Al-7Nb with similar strength was invented to replace Ti-6Al-4V alloys, metastable β-Ti alloys seem to be more perspective, due to reduced modulus of elasticity. The modulus of elasticity of bones is about 10-30 GPa [1] and bio implants are required to have as similar modulus of elasticity as possible. The modulus of elasticity of α+β-alloy Ti-6Al-7Nb is 100-110GPa [15] while the modulus of elasticity of metastable β-alloy Ti-15Mo in β-solution treated condition is about 78GPa [16].

Numerous metastable β-alloys were developed and are currently studied including: TNTZO (Ti-35.3Nb-7.3Zr-5.7Ta-0.7O), Beta C (Ti-3Al-8V-6Cr-4Mo-4Zr), Beta CEZ (Ti-5Al-2Sn-2Cr-4Mo-4Zr-1Fe) or Ti-15Mo studied in this thesis.

1.1.7 Ti-15Mo alloy

Ti-15Mo alloy contains 15 wt% of β-stabilizing molybdenum and therefore it is a metastable β-alloy. Its typical properties are listed in table 1.1. In solution treated condition, the Ti-15Mo alloy at room temperature contain β and ω_{ath}-phase [17].

α-phase precipitation may strengthen the material via precipitation hardening. The temperature range critical for α-phase precipitation is 500 °C – 750 °C. Also ω-phase formation strengthens the material via dispersion hardening, but it causes material embrittelment. ω-phase forms at temperatures 250 °C – 450 °C. The size and distribution of precipitates and particles is also important. Small and homogenously distributed α-phase particles are required to achieve the maximum strength.

However, in coarse-grained β-matrix the α-phase particles precipitate inhomogenously at preferential sites. Dense network of preferential sites such as grain boundaries, dislocations or ω-particles is therefore required.

Phase transformations in solution treated Ti-15Mo alloy were studied in [18] and with focus on ω-phase formation also in [17]. The effect of microstructure on phase transformations was discussed in [19, 20] where Ti-15Mo processed by high pressure torsion (HPT) and equal channel angular pressing (ECAP) was studied.

Table 1.1: Typical properties of metastable β-titanium Ti-15Mo alloy [16, 21]:

Density [g/cm^3]	4.96
Temperature of β-transus [°C]	774±14
Modulus of elasticity in tenstion [GPa]	78 (β) 105 (α+β)
Elongation [%]	20
UTS [MPa]	690

1.2 Ultrafine grained materials

Ultra-fine grained material is a polycrystalline material with equiaxed grains with the size smaller than 1 μm, homogenous microstructure and high fraction of high-angle grain boundaries (HAGB; misorientation higher than 15°). These materials have excellent mechanical properties such as high yield strength. The disadvantage is usually a reduced ductility [22].

The Hall-Petch relation:

$$\sigma_y = \sigma_0 + k_y d^{-\frac{1}{2}}, \tag{1.6}$$

where σ_y is yield strength, σ_0 is the friction stress of dislocation movement, k_y is a material constant and d is a grain size, describes the strengthening of the material by refinement of the grain size. It was determined independently by two physics: Hall and Petch in the 1950s [23, 24]. It presumes that the grain boundary is an obstacle of dislocation movement and dislocation pile-ups are formed at grain boundaries. Specific stress is necessary for passing of dislocations through grain boundary and continuation of deformation of the material. The dislocation pile-ups have a stress field which affects the neighboring grain. More dislocations can pile up in a larger

grain and form bigger stress field and consequently lower external stress is required to deform the crystal.

Ultra-fine grained microstructure can be reached by top-down or bottom-up approach [25]. Top-down approach includes methods of plastic deformation such as rolling or extrusion. However, only limited deformation can be inserted into material by these methods. Commonly used methods of severe plastic deformation (SPD) have advantage of preserving the sample shape and therefore theoretically unlimited repetition of the deformation. High deformation can be therefore imposed into the sample. The most common methods of SPD are high pressure torsion (HPT), equal channel angular pressing (ECAP) or accumulative roll bonding (ARB) [26]. Ultra-fine grained microstructure is in this case achieved by imposing severe deformation into the material and increasing the density of lattice defects. Dislocation cells, subgrains and finally grains are formed subsequently as a result of structure fragmentation.

On the other hand, during bottom-up approach bulk material is built by compaction of single atoms or from nanoscale blocks.

Ultra-fine grained structure is not an equilibrium microstructure and therefore it is not stable at elevated temperatures when recovery, recrystallization and grain growth occur.

1.2.1 Ultra-fine grained β-alloys

Favourable mechanical properties of metastable β-Ti alloys can be further improved by microstructural refinement. Both precipitation of α-phase and ultra-fine grained microstructure strengthen the material, but α-phase has the higher modulus of elasticity. Therefore, ultra-fine grained β-microstructure is advantageous for components in biomedicine where low modulus of elasticity is required. In other applications, such as aircraft industry, high strength is required which can be reached by both UFG microstructure and α-phase precipitation.

Metastable biomedical alloy Ti–29Nb–13Ta–4.6Zr (TNTZ) was prepared in [27] by cold rolling and subsequent high pressure torsion (HPT). Maximum achieved microhardness grew from about 220 HV to about 290 HV, however, the microstructure was inhomogeneous. The same alloy was prepared by HPT

deformation using higher number of HPT turns – the resulting microstructure is more homogeneous and the mechanical properties further improve. The maximum microhardness reached was about 300 HV with the modulus of elasticity of 60 GPa. TNTZ alloy prepared by HPT in α+β-condition achieves even higher microhardness of 450 HV, but the modulus of elasticity increases [28].

Preparation of metastable β-Ti alloys TIMETAL LCB and Ti-15Mo by 5 HPT turns in [29] resulted in UFG microstructure, the microhardness of 450 HV and 500 HV in Ti-15Mo alloy and TIMETAL LCB, respectively. The modulus of elasticity was about 90 GPa for both alloys. However, the microstructure was not homogeneous as the imposed deformation by HPT is not homogeneous and the reported mechanical properties correspond only for the periphery part of the sample where the imposed deformation is the highest [30, 31].

1.3 Recovery, recrystallization and grain growth

Recovery, recrystallization and grain growth is observed at elevated temperatures (about 500 °C for Ti alloys [32]), especially in severely deformed materials where the driving force is higher. Thermal activation of these processes depends on the homologous temperature T_m, which corresponds to the ratio of the given temperature to the melting temperature of the particular material.

At approximately 0.3 T_m, recovery occurs in pure metals. Point and line defects become mobile. Vacancies recombine with interstitials or annihilate in traps (dislocations, grain boundaries, sample surface) or form vacancy clusters. Dislocations arrange into energetically advantageous structures and form dislocation walls and low-angle grain boundaries (LAGB; misorientation lower than 15°) which form subgrains. This process is called polygonization. They may also recombine with dislocations of the opposite Burgers vector.

Recrystallization is a process of the formation of new undeformed grains by nucleation and growth. It occurs at interval wide range of temperatures from 0.4 T_m for pure metals up to 0.8 T_m for alloys. The preferential nucleation sites are typically triple points or regions with high dislocation density.

Finally, the grain growth is in some respect a continuation of recrystallization. If the recrystallized material is further annealed, the bigger grains start to consume the smaller ones. Unlike recrystallization, the driving force of grain growth is the lowering of the energy of grain boundaries. This process is time and temperature dependent according to the equation:

$$d^2 - d_0^2 = k_0 t \, exp(-\frac{Q}{RT}), \tag{1.7}$$

where d_0 is the initial grain size, d is the final grain size, k_0 is a material constant, t is time of annealing, Q is the activation energy of the process, R is the universal gas constant and T is the thermodynamic temperature.

2 Powder metallurgy

Powder metallurgy (PM) is an alternative approach of fabrication of metallic materials. Compared to conventional methods, where an ingot is prepared by casting, during PM the bulk material is compacted from powders. The properties of the final bulk material are affected by initial powder particles size, the shape and the morphology as well as by a method and parameters of compaction. The parameters of compaction must be optimized in order to achieve a compact, fully dense material.

Considering costs of conventional production of titanium, PM of Ti alloys is of significant interest and enjoys the current boom [33]. This approach allows the synthesis of materials and manufacturing of products which would be difficult or impossible to produce by conventional methods. An alloy can be prepared by mechanical alloying from elemental powders (or master alloys) which may be immiscible in melted condition due to low solubility. During mechanical alloying, supersaturated solid solution might be formed. Also parts from compounds with high melting temperature (e. g. tungsten carbide – 2780 °C [34]) may be more easily prepared by some methods of compaction. Currently extensively used method of additive manufacturing (AM), allows so-called net-shape production, which reduces manufacturing costs and material waste.

This thesis focuses on microstructural control of the studied Ti-15Mo alloy during cryogenic mechanical milling and subsequent compaction by spark plasma sintering.

2.1 Mechanical milling

The final properties of a bulk material prepared by powder metallurgy are affected not only by the method of compaction, but also by powder particles size, its morphology and internal microstructure. One way how to affect these properties is mechanical milling. Milling has been used for fragmentation of particles for centuries. In fact, in metals several processes can be observed during milling [35]:

- Fragmentation of powder particles which appears especially in brittle materials [35].
- The competitive process is cold-welding when particles join together. This process depends on the ductility and surface condition of powder particles. Process control agent, e. g. the stearic acid, may be used to prevent cold-welding. [35]

- Finally, powder particles may be plastically deformed during milling and UFG structure of powder particles can be reached [36].

Different types of milling devices such as vibrational mills, planetary mills or attritors can be used [35]. The vibrational mill is suitable for small amounts of powder. The planetary mill rotates around two axes and the milling is performed by interaction of powder with milling balls and tank walls. It has a lower efficiency in comparison with a vibrational mill, but higher amount of powder is produced. Finally, in an attritor, a mixture of powder and milling balls powder is propelled by a rotating shaft. Apart from commonly used stainless steel milling balls, heavier tungsten carbide balls can be used for milling of Ti alloys as shown in [37]. However, due to the contamination of the powder by tungsten carbide particles, stainless steel balls were used in this thesis [35, 37].

Cryogenic milling was originally developed for milling of biological samples which are brittle at cryogenic temperatures. Later it was found that this method is also suitable for milling of metals. Milling at cryogenic temperatures reduced times necessary for reaching small grain sizes [38, 39]. According to [35, 40] it is caused by suppressing of recovery and recrystallization. Milling tank can be cooled to cryogenic temperatures externally and milling occurs in air or in an inert atmosphere [41, 42]. Nevertheless, cryogenic milling can occur directly in a slurry of powder, milling balls and cryogenic liquid – either liquid argon (boiling temperature -186 °C) or liquid nitrogen (boiling temperature -196 °C). Milling in liquid nitrogen is, however, not suitable for titanium due to severe its contamination by nitrogen [37, 43].

2.2 Spark plasma sintering

Spark plasma sintering (SPS) is an advanced compaction technique also called Field Assisted Sintering Technology (FAST) or Pulse Electric Current Sintering (PECS).

During SPS, the powder is compacted by uniaxial pressure and Joule heating created by pulse electric current (in the order of kA) passing through the sintered sample [44]. A diagram of an SPS device is shown in Figure 2.1. A cylindrical graphite die containing two pistons is first filled with the powder. The chamber is then evacuated

and the pistons are pressed against each other while the graphite die is heated. Cooling can be controlled only by regulation of heating.

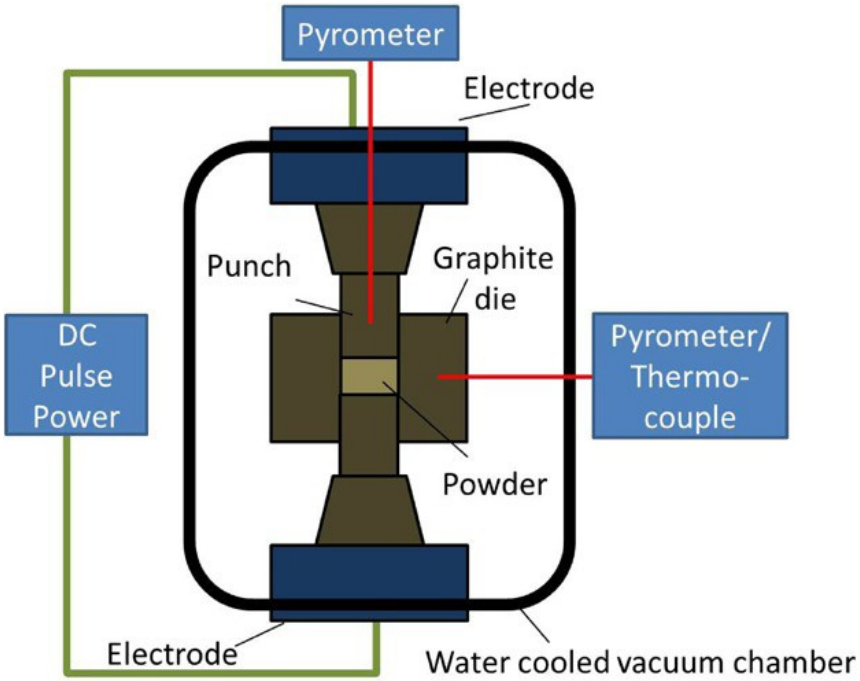

Figure 2.1: A diagram of SPS machine [44]

Other methods of compaction are, for example, the hot pressing (HP), the hot isostatic pressing (HIP) or the quasi-isostatic forging (QIP). In these methods the sample is heated from outside and typical sintering times are in the range of hours [45–49]. On the other hand, during SPS the powder particles are heated by Joule heating and the sufficient compaction is achieved in shorter times [44]. Furthermore, the heating rates of SPS are up to 1000 °C·min^{-1} [44]. The time of the whole SPS process is therefore much shorter, typically in range of minutes. This fact may help to reduce or to prevent recovery and recrystallization and to preserve the ultra-fine grained microstructure achieved by cryogenic milling. Interesting comparison is given in [50], where SPS for 5 minutes at 1000 °C was more efficient for compaction than vacuum sintering for 5 hours at the same temperature. However, SPS was less efficient in terms of alloy homogenization.

2.3 Milling and sintering of Ti alloys – literature review

In this section a literature review of cryogenic milling of titanium and of spark plasma sintering of titanium and its alloys with particular focus on metastable β-alloys.

Cryogenic milling of pure Ti has been investigated. The evolution of particles size and shape during milling was observed in [51]. While cold-welding was a dominant mechanism in the beginning of the milling process, the particle fragmentation occurred for longer milling times. The whole process resulted in the formation of equiaxed powder particles. The parameters of milling Ti powder, such as milling speed, milling time, milling medium, milling balls or process control agent were investigated in [37, 52]. The utilization of tungsten-carbide balls resulted in adverse contamination of Ti powder by tungsten-carbide particles. Similarly, the liquid nitrogen is not suitable as a milling medium due to contamination of Ti powder particles by nitrogen and their embrittlement [43].

Different methods of compaction of titanium and its alloys are thoroughly reviewed in [33]. Sintering of alloys can be generally done either from a pre-alloyed powder or from two or more elemental powders or from so-called master alloys. In the two latter cases, sintering serves also as an alloying process. While the temperature around the temperature of β-transus of particular alloy is often sufficient for compaction of pre-alloyed powder [50], sintering from elemental powder or from master alloys requires high temperatures and longer times to achieve a chemically homogenous structure. Especially β-stabilizing elements in metastable β-alloys have high melting temperature – vanadium (1910 °C), molybdenum (2623 °C) or niobium (2477 °C) – and low interdiffusion [2, 53]. Typical sintering temperatures required for the homogenization are 1100-1500 °C and typical sintering times are from 5 to 30 minutes [54, 55].

Pre-alloyed powder of commonly used TNZT (Ti-35Nb-7Zr-5Ta; temperature of β-transus 740 °C) alloy has been successfully sintered to 95 % of theoretical density at 800 °C for 15 minutes [50]. The same TNZT alloy was sintered at 1100 °C for 5 minutes from previously mechanically alloyed elemental powders [56]. Although sintering was done at a temperature above the temperature of β-transus, the resulting

microstructure is still two-phase, containing both α and β-phase. It can be a consequence of an insufficient cooling rate, which was not reported and can be as low as 30 °C/min [56] being insufficient to prevent α-phase precipitation. Another important factor is the contamination by oxygen and nitrogen which act as α-stabilizing elements and therefore increase the temperature of β-transus and significantly affect the α-phase precipitation [57]. These two elements also cause an embrittlement of the material. Milling and sintering in an inert atmosphere can prevent the contamination by nitrogen and oxygen.

Ti-26Nb-5Ag alloy was prepared by mechanically alloying in the planetary mill and subsequently spark plasma sintered at 1000 °C for 5 minutes. The final bulk material contained α and β-phase as well as martensitic α'' phase, despite sintering temperature was well above the temperature of β-transus [56]. The reason of α-phase precipitation was a very low cooling rate of 33 °C/min.

Ti-Mo alloys with different content of molybdenum (from 6 to 14 wt%) were prepared by spark plasma sintering from elemental powders at temperatures from 900 °C to 1350 °C for 5 minutes [55]. The cooling rate was not reported. The temperature required to achieve chemically homogeneous material increases with increasing Mo content from 1100 °C to 1300 °C. Ti-(6-12)Mo consists of α + β-mixture, while Ti-14Mo alloy contains only grain boundary α (GB α).

In this study, a pre-alloyed Ti-15Mo powder was used.

3 Aims of the thesis

The goal of the thesis is a complex characterization of Ti-15Mo alloy prepared by cryogenic milling and spark plasma sintering. The thesis focuses in detail on:

- Characterization of Ti-15Mo powder by advanced microscopic techniques and investigation of the influence of the cryogenic milling on the size, the shape and the microstructure of the powder particles.
- Optimization of sintering parameters aiming to produce compact bulk material with fine grained microstructure.
- Description of a complex methodology for the characterization of multi-phase metastable Ti alloy prepared by powder metallurgy.
- Investigation of mechanical properties of bulk Ti-15Mo alloy compacted by SPS from both initial and milled Ti-15Mo powder.
- Analysis of relations between processing parameters and achieved properties on the basis of current scientific knowledge about metastable Ti alloys and related physical processes.

4 Experimental material and characterization methods

4.1 Material preparation

Ti-15Mo alloy was procured from Carpenter Co., USA in the form of rods with a diameter of 10 mm and a length of 3 meters. The chemical composition of the initial bulk material is shown in Table 4.1.

Table 4.1: Default Composition of Ti-15Mo rods as specified by Carpenter Co:

Element	Content [wt%]
Ti	84.473
Mo	15.200
O	0.185
Si	0.090
Fe	0.030
N	0.014
C	0.007
H	0.001

Initial powder for the investigation was manufactured on demand by gas atomization at TLS Technik GmbH & Co. Spezialpulver KG, Germany.

4.1.1 Cryogenic milling

Cryogenic milling was performed in Union Process 01-HD attritor device with the stainless steel tank of the volume of 1400 cm^3 equipped with cryogenic cooling system with automatic temperature control. The system was cooled by liquid argon (temperature -186 °C) poured directly into the milling tank ("wet milling").

The Ti-15Mo powder was milled for 4 h and the milling rate of 700 RPM. Stainless steel balls (the density of 7.8 g/cm^3) of the size of 6.35 mm in diameter and ball-to-powder ratio of 16:1 were used as a grinding medium.

Stearic acid (SA) was used as a control agent to prevent cold-welding. 1.8 g of stearic acid was added to 180 g of Ti-15Mo.

4.1.2 Spark plasma sintering

Spark plasma sintering was performed at the Institute of Plasma Physics of the Czech Academy of Sciences in the SPS 10-4 furnace made by Thermal Technology LLC, USA. The powder was sintered in a graphite die and the compacted samples had the shape of a cylinder with the diameter of 20 mm and height of about 7 mm. About 11 g of powder were used for each sample. The sintering pressure was 80 MPa.

Both non-milled and milled powders were sintered at temperatures of 750 °C, 800 °C and 850 °C for sintering times 0, 1, 3 and 6 minutes in different combinations. Prepared samples are listed in Table 4.2. 0 min means that the sample was heated to the desired temperature and the heating was immediately turned off without holding. A representative example of the record of sintering conditions is shown in Figure 4.1 for the sintering temperature of 850 °C and the time of 3 minutes. Other samples were prepared by analogous procedures, namely: the sample was heated to 50 °C below the desired temperature in 1 minute (the heating rate differs for different sintering temperatures) and then heated up to the sintering temperature in 30 s (the heating rate of 100 °C/min) to avoid overshooting the desired temperature. The temperature was measured by a thermocouple inserted into the hole in the bottom of the lower graphite piston and located 4 mm from the sample.

Samples i750/3, i850/3, m750/3 and m850/3 were selected for further investigation to establish the effect of prior milling and the effect of sintering temperature on microstructure, chemical contamination and mechanical properties.

Table 4.2: An overview of used sintering conditions and respective labels of samples for both initial and milled powder:

Labels of sintered initial powders				Labels of sintered milled powders			
time/temp.	750 °C	800 °C	850 °C	time/temp.	750 °C	800 °C	850 °C
0 min	x	i800/0	x	0 min	x	m800/0	x
1 min	i750/1	i800/1	i850/1	1 min	m750/1	m800/1	m850/1
3 min	i750/3	i800/3	i850/3	3 min	m750/3	m800/3	m850/3
6 min	x	i800/6	x	6 min	x	m800/6	x

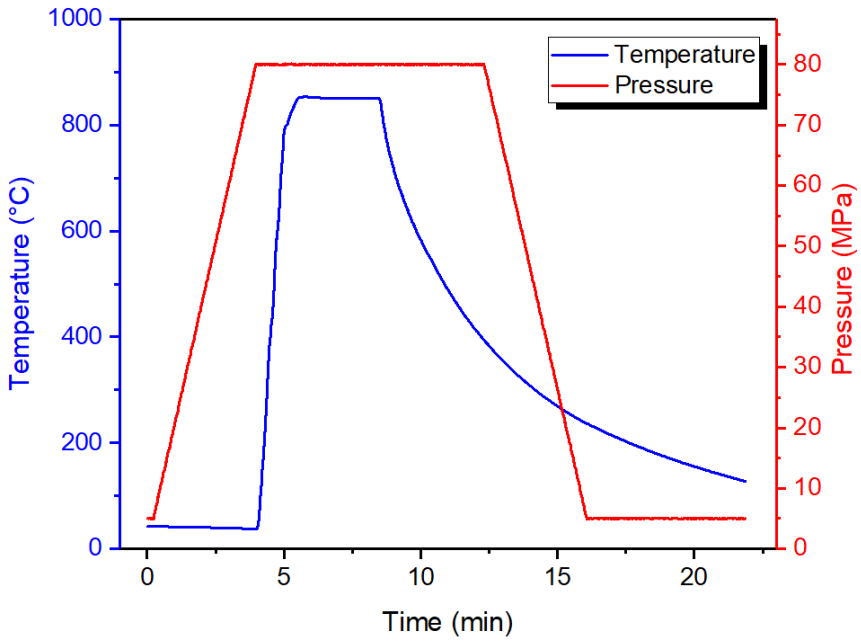

Figure 4.1: An example of the record of sintering conditions (here shown for the sintering temperature of 850 °C and the time of 3 minutes)

Cooling can be controlled only by regulation of heating; in this study, the cooling rate was left uncontrolled and the cooling rate decreased exponentially as shown in Figure 4.1.

4.2 Sample preparation

Powders for SEM observation were put on a conductive foil and observed without polishing. In order to observe the cross section of milled powder particles, the powder was hot mounted in an epoxy resin and grinded and polished in the same way as bulk samples (described below).

SEM observations, X-ray diffraction (XRD) and microhardness measurement were performed on a vertical plane. Orientation of a specimen within the sample is schematically displayed in Figure 4.2 as a dark grey part. All samples were mechanically grinded on SiC grinding papers up to #2400 grit and polished by three steps of vibratory polishing in vibratory polisher. Suspensions of 0.3 μm and 0.05 μm alumina and 0.04 μm colloidal silica were used. Samples sintered from milled powder were additionally polished in the ion polisher Leica EM RES102.

Dog-bone shaped flat specimens for tensile tests were cut from plates with the thickness of 1 mm and height of 7 mm from the middle of a sintered tablet (see

Figure 4.2). The gauge length was 5 mm, the width and the thickness approximately 1.2 mm and 1 mm, respectively.

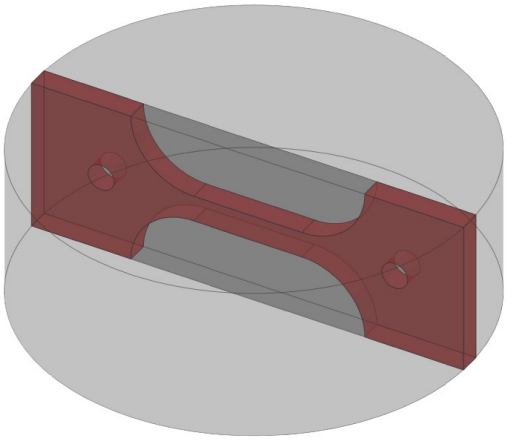

Figure 4.2: Dog-bone shaped sample for tensile tests

Cylinders with the height of 5 mm and the diameter of 3.5 mm were used for compression tests. The axis of the cylinder for compression test was perpendicular to the direction of sintering.

Samples for transmission Kikuchi diffraction (TKD) were prepared by focused ion beam (FIB). The details of their preparation are described below.

4.3 Scanning electron microscopy

Microstructure of both powders (initial and milled) and sintered samples were studied using scanning electron microscope FEI Quanta 200F operated at 10 kV. The source of electrons in this microscope is a field emission gun (FEG). Emitted electrons (primary beam) are accelerated by a voltage of 10 kV before they interact with atoms in sample. Several types of signal are observable – back-scattered electrons, secondary electrons or characteristic X-ray radiation.

Back-scattered electrons (BSE) are electrons from primary beam which are elastically scattered by the atoms of the sample and can be detected by BSE detector. The intensity of back-scattered electrons depends on several factors. Elements with higher atomic number have higher electron density and therefore the intensity of back-scattered electrons is higher and their probability to leave the sample and to be detected is also higher. The intensity of back-scattered electrons depends on the type

of the atom and BSE signal provides therefore the information about the chemical composition of the sample. This phenomenon is called *Z-contrast* and in case of Ti alloys is mainly used to distinguish α and β-phases.

Another type of information carried by BSE is based on the local orientation of crystalline planes with respect to the incident electron. Differently orientated grains with respect to the primary beam scatter the beam in a different way and are therefore seen in different grey level in a BSE micrograph and form so called *channelling contrast*.

Electrons from the primary beam can interact with the sample by inelastic scattering and a *secondary electron* (SE) from an outer atomic shell can be emitted. These secondary electrons have lower energy in comparison with primary or back-scattered electrons and therefore only SE scattered by atoms located near the surface can reach the surface and be detected. The intensity of SE depends also on the angle of incidence of the primary beam on the surface and SE holds therefore the information about the topography of the specimen, creating so called *topographical contrast*. Figure 4.3 displays the bulk penetration of the primary beam and the volume of the sample from which SE, BSE and characteristic X-rays may be detected.

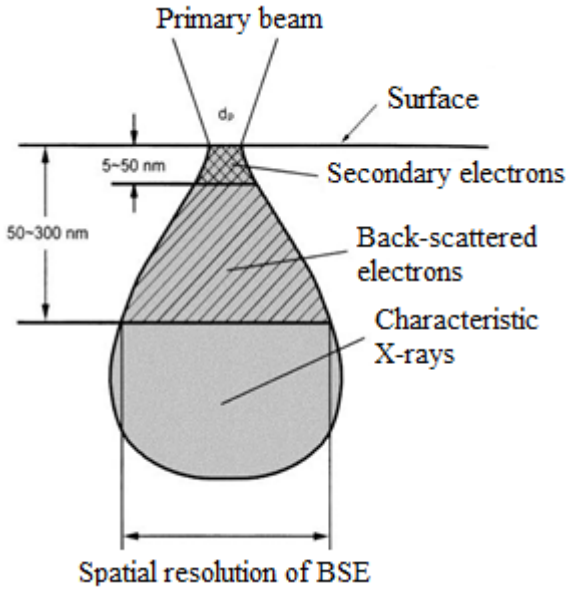

Figure 4.3: Bulk penetration of primary electrons

If an electron from an inner atomic shell is knocked out by the incident beam from the atom, the excited atom is immediately deexcited by filling the vacant place by an

electron from one of the outer shells. This process is accompanied by the emission of the X-ray photon whose energy is given by the difference of the energies of both atomic shells forming so called, *characteristic X-ray* signal. The energy of the signal is characteristic for the particular atom and therefore a chemical composition can be determined both quantitatively and qualitatively by measuring the energy of characteristic X-rays. The method is called energy dispersive X-ray spectroscopy (EDX) and allows mapping the local chemical composition of the sample.

4.3.1 Electron back-scattered diffraction

Electron back-scattered diffraction (EBSD) is a method which allows determining automatically the orientation of the material a measured point on the sample. EBSD scan contain the information about microstructural features as, e.g. the grain size, the texture, misorientation of grains or subgrains etc.

The orientation in each measured point is determined from the pattern of Kikuchi lines. Kikuchi lines are formed by elastic scattering of inelastically scattered electrons as schematically shown in Figure 4.4.

Primary electrons are firstly scattered inelastically (but they do not lose more than 10 % of their energy) and then elastically. The intensity of inelastically scattered beam is dependent on the direction of scattering. It is highest in the direction of primary beam and it decreases with increasing angle of scattering. Let primary beam of wave length λ inelastically scatter in point A, then waves in two directions – 1 and 2 – comply with the Bragg's diffraction condition:

$$\lambda = 2d_{hkl}sin\theta_{hkl}, \tag{4.1}$$

where d_{hkl} is interplanary distance and θ_{hkl} is Bragg's angle (see Figure 4.4). Therefore, waves 1 and 2 have got different intensity dependent on deviation from the initial direction. In our case wave 1 has a lower intensity than wave 2 (see Figure 4.4). In point B a part of wave 2 is scattered in the direction of wave 1. Let us mark the scattered fraction 21 and the transmitted fraction 22. Similarly, for wave 1 and point C It holds:

$$\begin{gathered} I_2 > I_1 \implies I_{21} > I_{12}, \\ I_2 - I_{21} + I_{12} < I_2;\ I_1 - I_{12} + I_{21} > I_2. \end{gathered} \tag{4.2}$$

Therefore, there is a maximum in a direction 1 and minimum in a direction 2 on a background of intensity I_2. Figure 4.4 is a projection of the real situation into plane. In three dimensions the electrons are scattered into cones and the Kukuchi lines are an intersection of the cone with plane of the screen. “Line” is therefore an approximation, Kikuchi “lines” are in fact conic sections. An example of Kikuchi lines pattern collected from a point on the sample surface using the EBSD camera is shown in Figure 4.5.

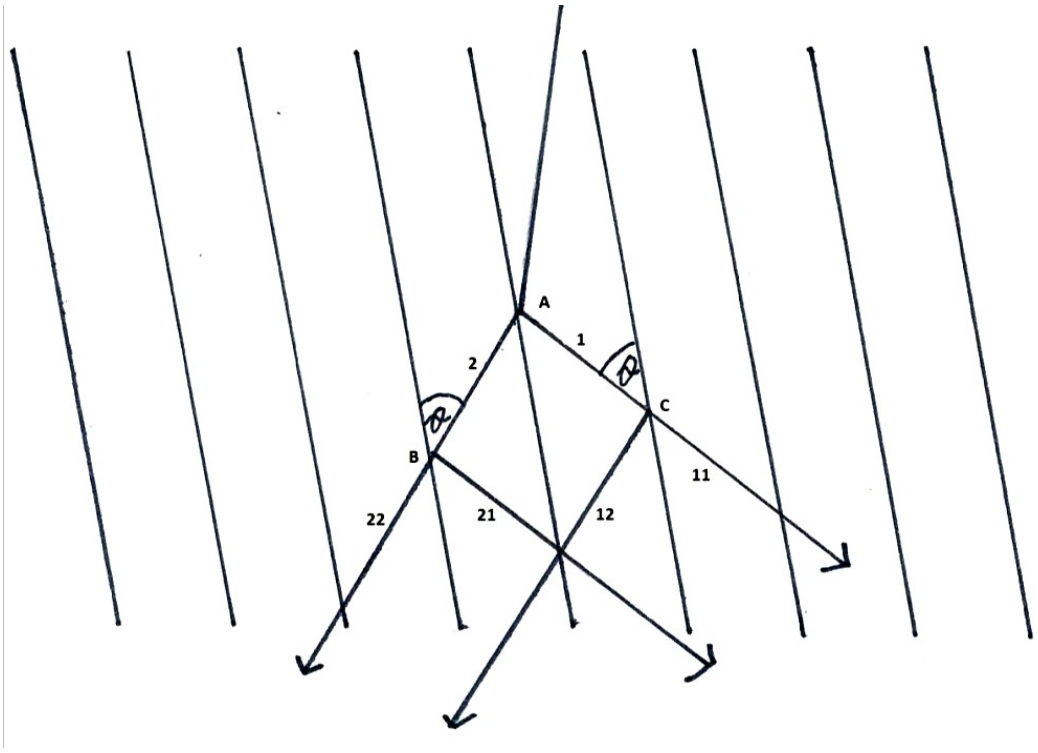

Figure 4.4: A principle of Kikuchi lines formation

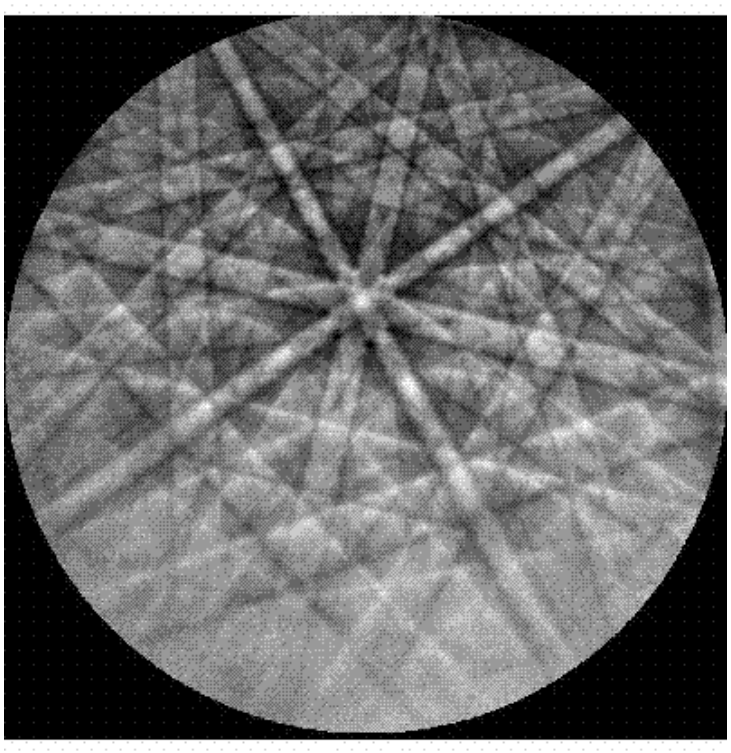

Figure 4.5: An example of Kikuchi lines pattern [58]

Each Kikuchi line corresponds to the system of crystallographic planes. Mutual orientation of three Kikuchi lines is necessary for the determination of crystallographic orientation of the point. The stereographic projection of the plane which is parallel to the surface, i.e. the orientation, in the measured point is usually displayed in a colour code in the orientation triangle shown in Figure 4.6 for cubic structure. The result of EBSD is inverse pole map figure (IPF)

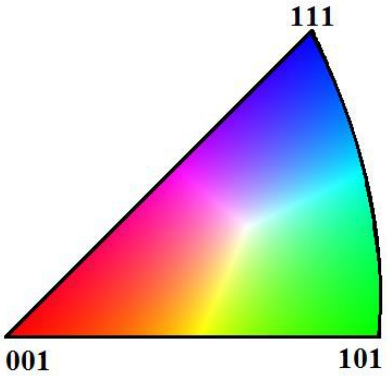

Figure 4.6: Orientation triangle of cubic structure

In order to achieve a maximum signal, the sample was tilted by 70° to the EBSD camera screen. This however results in high interaction volume and lows the resolution in both lateral (perpendicular to the primary beam) and longitudinal

(parallel to the primary beam) direction. The typical resolution achieved by EBSD is tens of nanometres.

The EBSD map was made by scanning electron microscope Zeiss Auriga equipped with a field emission gun (FEG), focused ion beam (FIB) and camera for electron back-scattered diffraction (EBSD) at accelerating voltage 10keV with the acquisition step of 20 nm. The resulted inverse pole map figure was cleaned by standard methods.

4.3.2 Transmission Kikuchi diffraction

Transmission Kikuchi diffraction (TKD) is also called transmission EBSD (transmission electron back-scattered diffraction – tEBSD). This name, however, is improper, because the terms “transmission” and “back-scattered” are opposites.

The method was suggested by Keller and Geis in 2012 to improve the spatial resolution of EBSD [59]. The signal is formed on the same principle as during EBSD (described above) and is detected by the same EBSD camera. However, unlike during EBSD, the forward scattered electrons passed through a thin sample are detected.

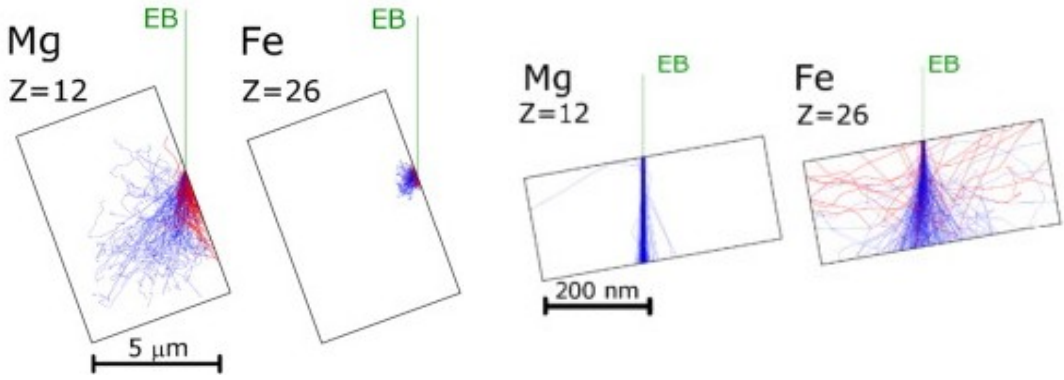

(a) EBSD (b) TKD

Figure 4.7: Simulated electron trajectories in EBSD and TKD configurations at 20 keV. Red trajectories show back-scattered electrons, blue ones transmitted electrons or those stopped within the material. Note the significantly different scale of both images [60].

The principle is shown in Figure 4.7 (note different scale of figures). The first advantage of TKD is the lower tilt angle (20 °C) which improves the lateral resolution. Due to a small thickness of the sample the beam leaves the sample before

the interaction volume (Figure 4.3) is widened. As a consequence the theoretical resolution of 2.5 nm can be reached [61] by TKD.

Thin lamella, typically prepared by focused ion beam (FIB) is inserted to standard SEM equipped with an EBSD camera. The scheme is shown in Figure 4.8. The specimen is tilted by 20°.

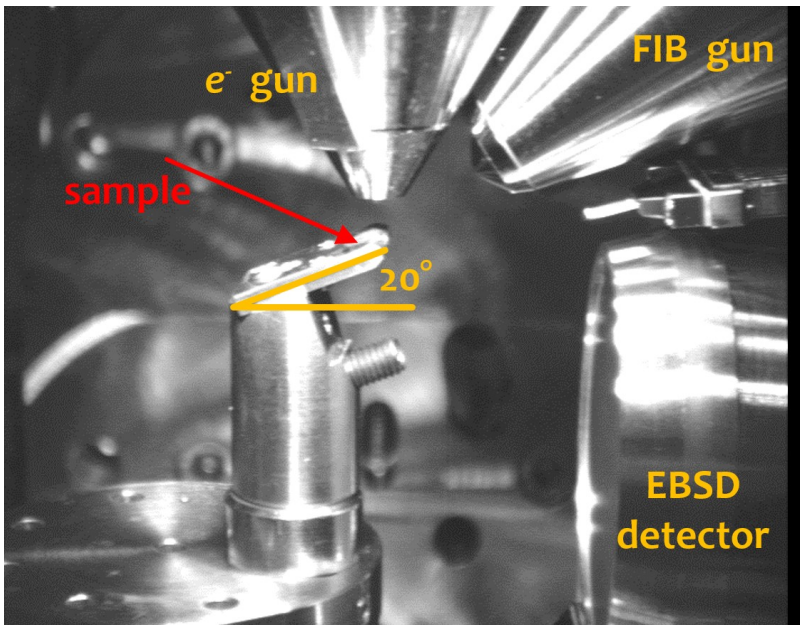

Figure 4.8: Geometry of TKD in the chamber of Auriga Zeiss Compact FIB-SEM [62]

4.3.3 Focused ion beam

Samples for transmission Kikuchi diffraction (TKD) were prepared by focused ion beam (FIB) and gas injection system (GIS). FIB uses accelerated ions of gallium for nano- or micro-milling while GIS allows a deposition of nano- or micro- structures on the surface of FIBbed lamella.

For the purpose of transmission Kikuchi diffraction, a lamella was made by FIB. Platinum from GIS was deposed on the top of the lamella as a protection. The lamella was cut by FIB operating at 30 kV and gradually thinned by decreasing current from 7.5 nA to 50 pA. The final thickness of the lamella was around 100 nm. The lamella was moved from the sample to the holder before final thinning by micromanipulator. The platinum from GIS serves also as glue for sticking the lamella to the micromanipulator and to the holder.

In principle, conventional methods of transmission electron microscopy (TEM) sample preparation can be used for preparing a sample for TKD, but making a lamella by FIB and GIS is faster and easier. Furthermore, orientation of the lamella with respect to the sample can be controlled during the preparation by FIB.

4.4 X-ray diffraction

The principle of X-ray diffraction (XRD) is the interaction of primary X-ray beam with periodic atomic planes in crystalline sample. The constructive interference is observed when Bragg's diffraction condition (4.1) is fulfilled. The result of XRD measurement is a diffraction pattern – dependency of measured intensities of X-ray signal on the 2θ angle.

The detected intensity I_{hkl} is proportional to $|F_{hkl}^2|$, where F_{hkl} is the structural factor. It contains a sum of scattered intensities by singular atoms and determines for what angles a constructive interference (maximum) will be observed. Every maximum corresponds to a specific system of crystallographic planes. From peak positions the symmetry of crystalline structure (the phase) and lattice parameters can be determined.

The integral intensity of the peaks is proportional to the volume fraction of individual phases. However, the determination of quantitative phase composition may be complicated due to other factors affecting the intensity, such as the texture T_{hkl} factor. Texture is a preferred crystallographic orientation. If some system of planes is more probably oriented parallel to the sample surface, then the peak corresponding with this system will have the higher intensity.

Another factor which can be determined in powder XRD is a peak broadening. Theoretically, an XRD peak is a delta function. Peak broadening is caused by aperture resolution and by non-ideal sample. The peak is further broadened by lattice defects, microstrains in sample and small crystallite (coherently scattering zone) size.

XRD measurements were performed on a Bruker D8 Advanced diffractometer in Bragg-Brentano geometry using Cu K_α radiation, λ = 1.54051 Å, variable divergence slits, and a Sol-X detector. Bragg-Brentano geometry is an arrangement in which the incident and diffracted beams are focused on a circle with the measured sample in

the middle. Diffraction patterns were collected at room temperature in the 2θ range from 30° to 130° with a step size of 0.02° and an exposure time of 5 s/step.

The patterns were fitted and refined using the program Jana2006, employing le Bail algorithm with a pseudo-Voigt profile, and ten to fifteen terms of Legendre polynomials for the background [63]. As ω and α-phase peaks have lower intensity in comparison with β-peaks, a special approach to fitting was employed. β-peaks were fitted first, then α-phase (if present) was added into fitting procedure and its parameters were refined. Afterwards, ω-phase was added and peak positions were fitted. Then, the fitted β-peaks overlapping with the ω-phase peaks were excluded from the refinement, allowing broad and less intense ω-phase peaks to be independently and properly refined. Finally, parameters of β and α-phase were finely refined with fixed ω-phase parameters to achieve the best possible fit.

4.5 Carrier gas hot extraction

Carrier gas hot extraction (CGHE) was used for the determination of the content of light elements (hydrogen, nitrogen and oxygen) in the material.

Helium is used as a carrier gas for measuring of the content of O, N and H. The sample is precisely weighted, placed into a nickel capsule and heated up to high temperature (up to 3000 °C). The gases are released from the sample – nitrogen in the form of N_2, and hydrogen as H_2. Oxygen reacts with crucible and forms CO which can be directly detected by IR spectroscopy. More often it is further catalysed to CO_2. Similarly, H_2 is usually catalysed to H_2O. Gases are afterwards chromatographically separated and measured by thermal conductivity detector which compares the thermal conductivity of the measured gas with the carrier gas.

The measurement of CGHE was performed at TU Bergakademie Freiberg, Germany.

4.6 Mechanical properties measurement

4.6.1 Microhardness measurements

Microhardness measurement is an easy and fast method of material characterization and provides a simple comparison of different samples.

Microhardness was measured by Vickers method employing the microhardness measurement device Qness Q10a. A diamond indenter is pressed into the sample by a defined force F for a defined time t. The geometry of the indenter is shown in Figure 4.9. The indenter has a shape of a pyramid with the angle 136° between opposite faces. It makes an imprint. The length of diagonals of the imprint is automatically measured and its area A is counted according to the formula:

$$A = \frac{d^2}{2\sin(136°/2)} \approx \frac{d^2}{1.8544}, \tag{4.3}$$

where d is an arithmetic mean of the diagonals. The microhardness is then calculated from the formula:

$$HV = \frac{F}{A}, \tag{4.4}$$

where F is a kilogram-force (kgf).

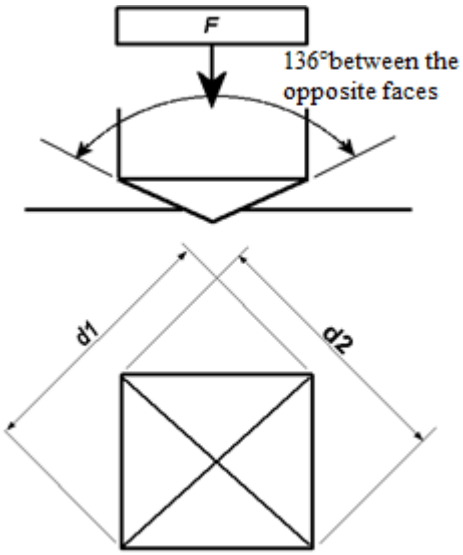

Figure 4.9: The geometry of microhardness indentation [64]

The microhardness of each sample was measured by F = 0.5 kgf (HV 0.5) and the dwell time of 10 s. 30 indents were made for each sample.

4.6.2 Deformation tests

During deformation tests the sample is deformed at the constant deformation rate and the change in length ΔL and load F is measured. The output is a dependence of stress on strain (so called stress-strain curve). Strain is calculated according to the formula:

$$\varepsilon = \frac{\Delta L}{L_0}, \tag{4.5}$$

where L_0 is the original sample length. The stress is defined as:

$$\sigma = \frac{F}{S_0}, \tag{4.6}$$

where S_0 is the initial cross section of the sample. These formulae hold for small deformation and are called engineering stress and strain.

When the stress-strain curve starts to deviate from elastic line the sample starts to deform plastically. The characteristic parameter, called the *yield stress* corresponds to the stress at 0.2 % of plastic strain and is marked as $\sigma_{0.2}$.

Formulae for engineering stress and strain are not appropriate for large deformation, because they are derived from initial sample dimensions. However, these dimensions change during deformation. Actually, the following formula for so called true strain (ε_{true}) is more proper and holds for whole deformation:

$$d\varepsilon = \frac{dL}{L} \implies \varepsilon_{true} = \int_{L_0}^{L} \frac{1}{L} dL = ln \frac{L}{L_0} \tag{4.7}$$

Considering equation (4.5) the relationship between engineering and true strain can be determined:

$$\varepsilon_{\text{true}} = \ln(1 + \varepsilon) \tag{4.8}$$

If we assume the constant sample volume during deformation, it holds:

$$S_0 \cdot L_0 = S \cdot L \implies \frac{S}{S_0} = \frac{L_0}{L} \tag{4.9}$$

From equations (4.6) and (4.9) we can derive also relationship between engineering and true stress:

$$\sigma_{\text{true}} = \sigma(1 + \varepsilon) \tag{4.10}$$

Another characteristic value is the *ultimate tensile strength* (σ_{UTS}). It is the maximum on the engineering stress-strain curve. During further deformation the sample necking occurs and the strain is no longer homogeneous and is localized to the neck and the specimen breaks shortly.

Both compression and tensile test were performed at Instron 5882 machine. The constant crosshead velocity was 0.03 mm/s. The gauge length of 5 mm (tensile samples) and the height of cylindrical compression samples of 5 mm results in the initial strain rate of $\dot{\varepsilon} = 10^{-4}\ s^{-1}$ for both tensile and compression tests.

5 Results

5.1 Powders

5.1.1 Microstructure observed by a SEM

Both initial and milled powders were observed by SEM. Powder particles before milling (Figure 5.1 left) are ball shaped and their size ranges from several micrometres up to thirty micrometres. The size is much bigger than that declared by the manufacturer (< 20 μm). On the other hand, powder particles after milling (Figure 5.1 right) are disc shaped. They are not significantly refined – the diameter of the disc is up to a hundred of micrometres – but deformed by mechanical milling.

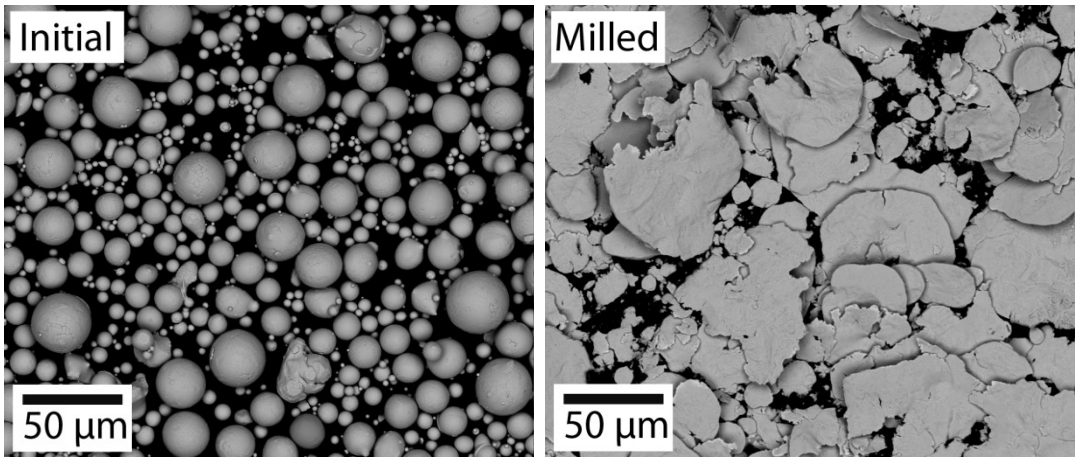

Figure 5.1: SEM micrograph (SE) of initial powder (left) and milled powder (right)

The thickness of milled powder particles can be estimated from SEM observations of powder particles hot mounted in an epoxy resin shown in Figure 5.2. The estimated thickness, about 2-3 μm, is inaccurate due to random orientation of powder particles with respect to the plane of observation. Therefore, the observed area may not correspond to the perpendicular cross section.

Figure 5.3 displays mainly chemical contrast within an initial powder particle. The black areas are Mo depleted areas, which were formed during solidification of the powder during gas atomization.

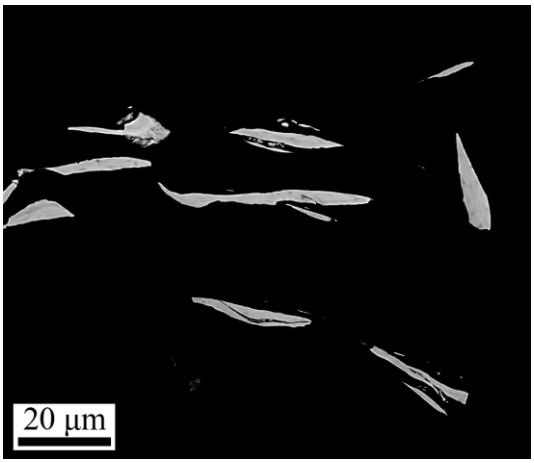

Figure 5.2: Milled powder particles hot mounted in an epoxy resin – cross-section

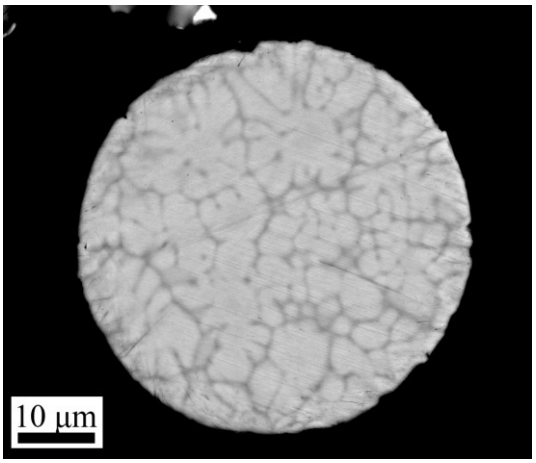

Figure 5.3: Chemical contrast of initial powder particle

5.1.2 Chemical contamination measured by CGHE

Chemical contamination of initial and milled powders by oxygen, hydrogen and nitrogen was measured by CGHE. Contamination by all measured elements increased during milling.

Table 5.1: Contamination of initial and milled powder by oxygen, hydrogen and nitrogen in weight percent

Powder	Oxygen	Hydrogen	Nitrogen
Initial	0.198	<0.001	0.014
Milled	0.784	0.147	0.030

5.2 Bulk sintered material

5.2.1 Microstructure of sintered initial powder

5.2.1.1 Overview SEM imaging

Microstructure of sintered samples was observed at different magnifications.

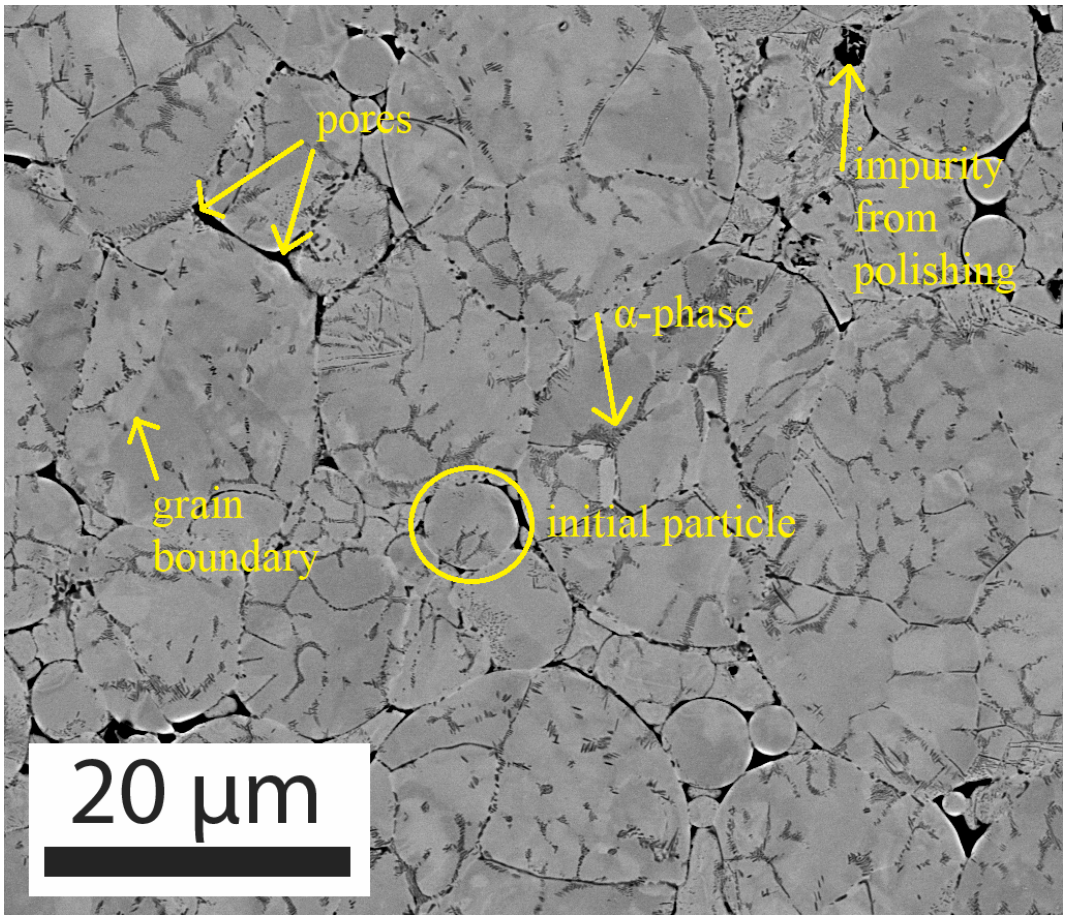

Figure 5.4: Representative SEM micrograph (BSE)

In Figure 5.4, a representative SEM micrograph (BSE) of sample sintered at 750 °C for 1 minute from the initial powder is shown. Several features can be observed in the micrograph. The larger black areas are mostly pores. Pores are observed around initial powder particles and due to them, round initial particles can be still observed. Impurities from polishing contain light elements and therefore impurities appear black as well as pores and it is difficult to distinguish between them from a BSE image. We can use SE micrograph instead. Due to the topological contrast pores remain black but impurities are white (Figure 5.5 bottom). Small black lamellar α-phase precipitates are visible thanks to element partitioning. β-stabilizing molybdenum is expelled from α-phase precipitates to β-matrix and therefore α and β-phase have slightly different chemical composition and are visible by Z contrast. Finally, some grains are visible by channelling contrast, but the contrast is very weak.

Overview SEM micrographs of initial powder sintered at selected conditions are shown in Figure 5.5. While phase composition is well seen in BSE micrographs due to chemical contrast, pores are better visible in SE micrographs. Therefore, the same areas of the chosen samples i750/3 and i850/3 are displayed in both BSE and SE micrographs in Figure 5.5. BSE micrographs are shown in the top of the figure while SE ones in the bottom.

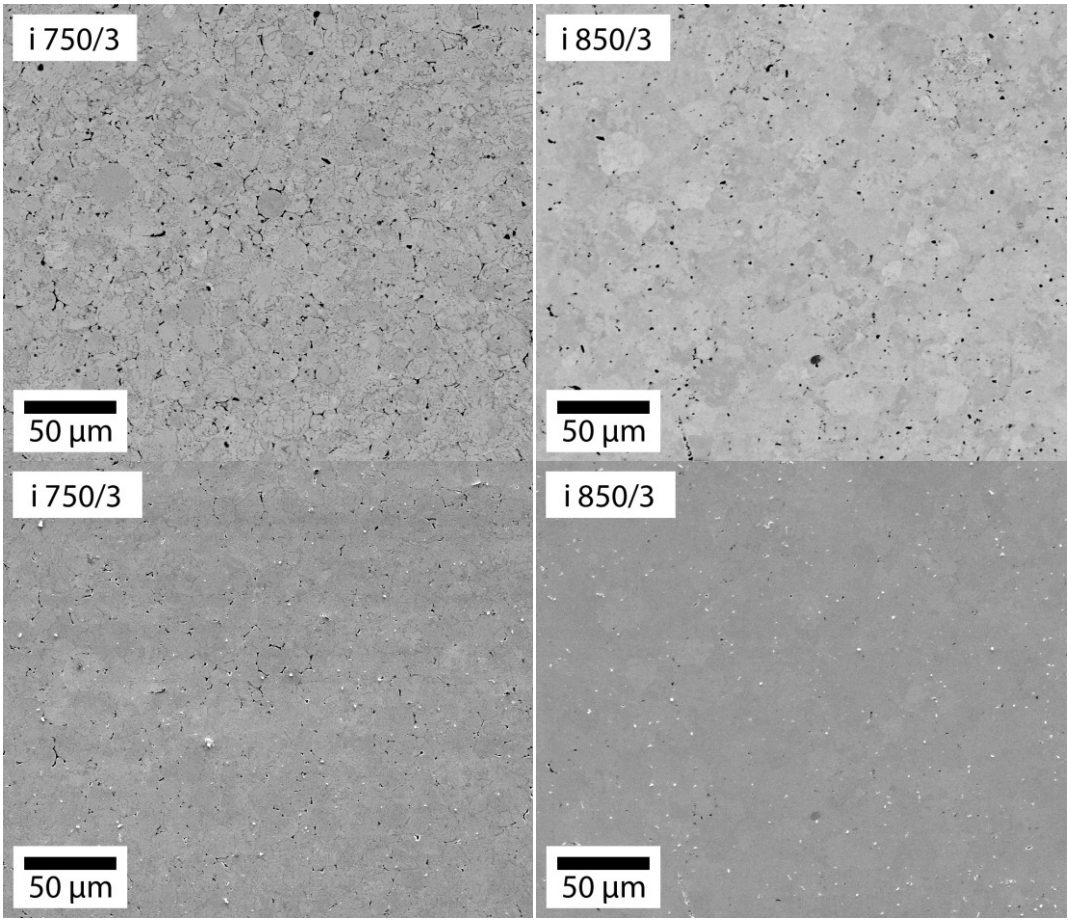

Figure 5.5: Overview of initial powder sintered at 750 °C (left) and at 850 °C (right) for 3 minutes captured (BSE – top and SE – bottom)

Initial powder sintered at 750 °C for 3 minutes (i750/3) is shown on the left of Figure 5.5 and non-milled powder sintered at 850 °C for 3 minutes (i850/3) is shown on the right of Figure 5.5. In both samples, black areas in BSE figures are mainly pores, but few remnants from polishing are also present. They can be well distinguished in SE micrographs. In the sample sintered at 750 °C, initial powder particles are still recognisable due to pores localized between them. Grain structure can be also partly observed in BSE micrographs due to channelling contrast. In the

SE micrograph of sample sintered at 850 °C, impurities from polishing are mainly seen in topological contrast.

5.2.1.2 Homogeneity of porosity of sintered initial powder

The homogeneity of sintered samples in terms of porosity was studied. Schematic representation of studied areas is provided in Figure 5.6.

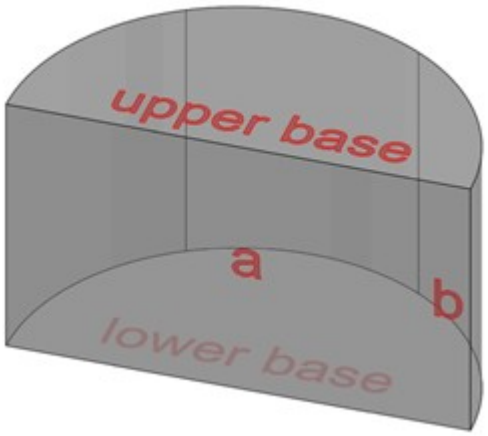

Figure 5.6: Schematic representation of studied areas – (a) central part and (b) periphery part of the sample

Porosity was studied in samples prepared from the initial powder sintered at 800 °C for 0, 1, 3 and 6 minutes as shown in Figure 5.7 (SE). White dots (especially in the i800/0 sample) are impurities from polishing while black areas are pores. Samples are significantly better sintered (i.e. with lower porosity) in the center part. Center part shows low porosity already for short sintering times while the periphery part is porous and initial round particles can be still recognized for short sintering times (0 and 1 minute). Decreasing fraction of pores with increasing time of sintering is observed especially in the periphery part of the specimen.

Porosity was studied also for milled powder sintered at 750 °C - 850 °C. However, almost zero porosity was observed throughout the samples, including samples sintered at low temperatures and short times (m750/1 and m800/0).

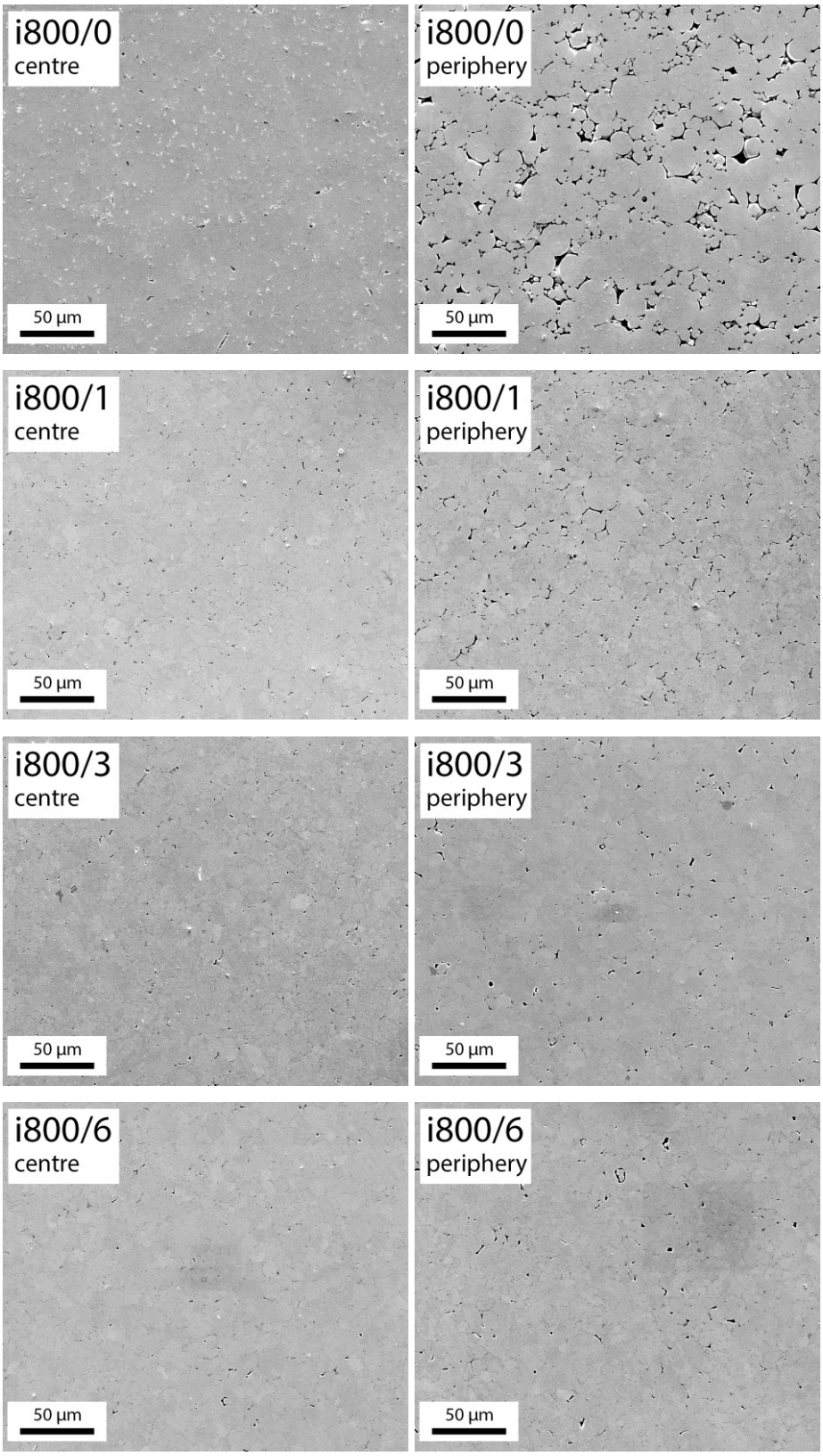

Figure 5.7: Homogeneity of porosity depending on the time of sintering. Centre part (left) and periphery part (right) of the sample.

5.2.1.3 Detailed SEM imaging

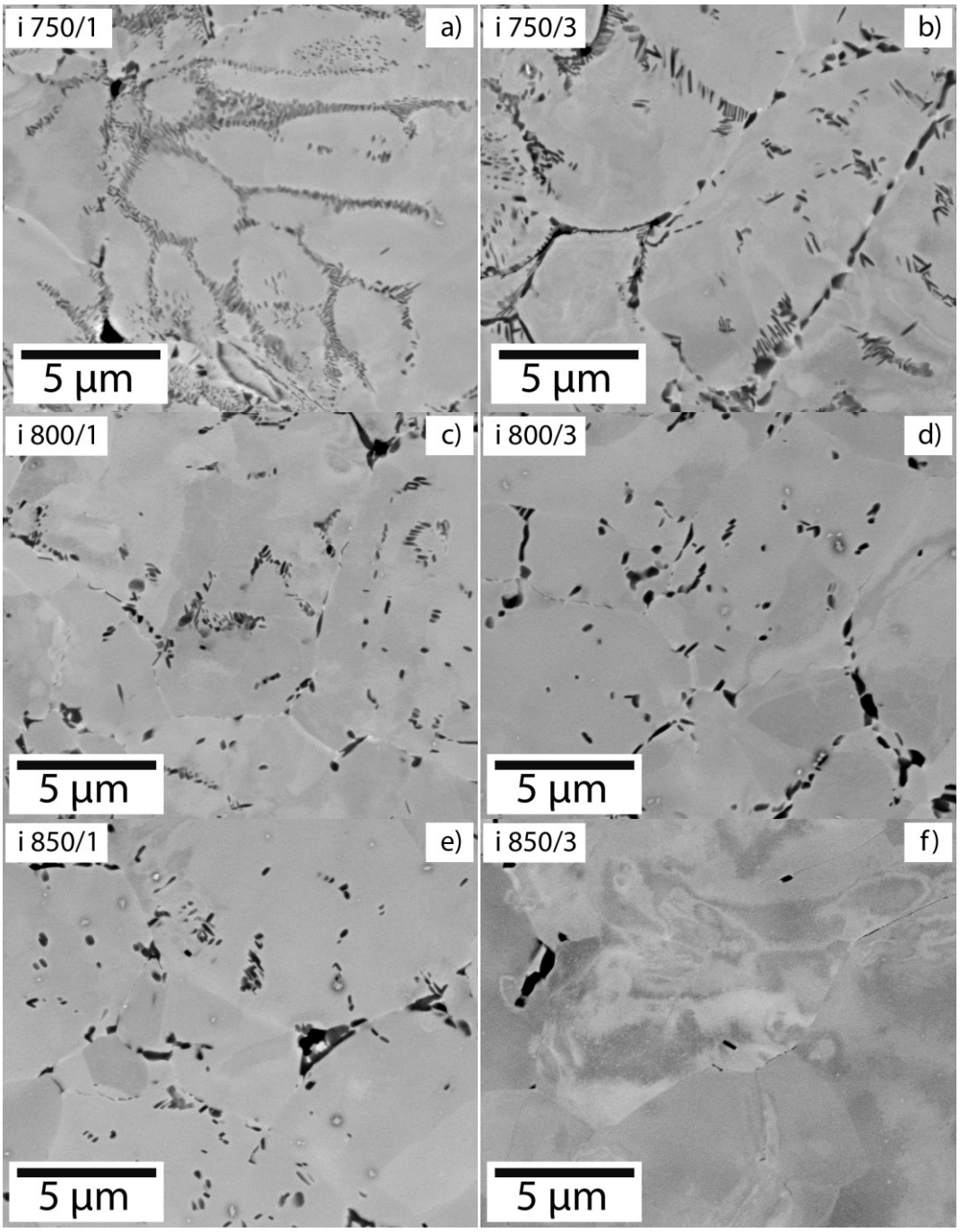

Figure 5.8: SEM micrographs (BSE) of non-milled samples sintered at 750 °C (top), 800 °C (middle) and 850 °C (bottom) for 1 (left) and 3 (right) minutes

Detailed BSE SEM micrographs of sintered non-milled powder are shown in Figure 5.8. The black areas correspond mainly to α-phase as proved below by EBSD for the i750/3 sample. In the i750/1 sample, α-phase precipitates are small, lamellar and are present in the Mo depleted areas, which were formed during solidification of

powder during gas atomization (see Figure 5.3). Bigger α-phase particles are present between original powder particles. With increasing sintering time and temperature, the fraction of α-phase decreases while the size of α-phase particles increases.

5.2.1.4 Microstructure observation by EBSD and EDX

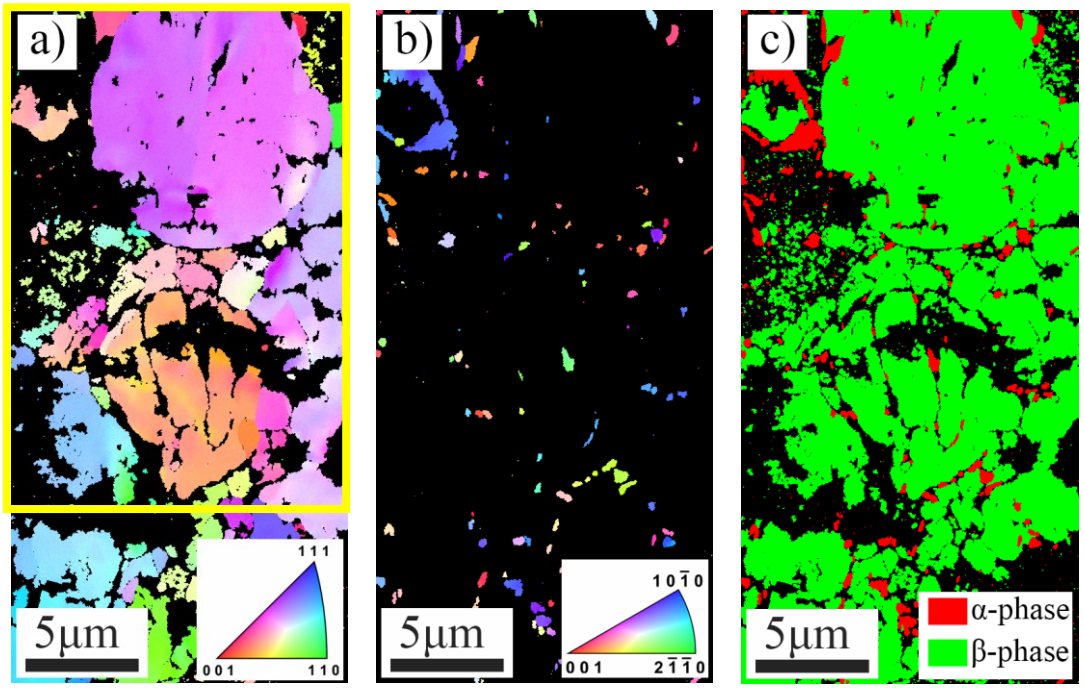

a) α-phase b) β-phase c) Phase map

Figure 5.9: Inverse pole figure map of sample i750/3 – a) α-phase, b) β-phase, c) phase map

EBSD scans were done for initial powder sintered at 750 °C for 3 minutes and the resulting IPF maps are shown for β-phase and α-phase in Figures 5.9 a) and 5.9 b), respectively. The phase map is shown in Figure 5.9 c). It is observed in Figure 5.9 a) (β-phase), that small (~5 µm) initial powder particles are single crystalline. The same area of the sample was investigated by EDX. EDX maps for Ti and Mo along with SE micrograph are shown in Figure 5.10. The yellow rectangle in Figure 5.9 a) corresponds to yellow rectangle in Figure 5.10 c). By comparing Figure 5.9 b) (α-phase) and Figure 5.10 a) (Ti content) it is obvious that positions of α-phase particles coincide with the Ti enriched areas. Clearly, Ti enriched areas are Mo depleted, as observed in Figure 5.10 b) α-phase particles contain relatively lower amount of β-stabilizing molybdenum and higher amount of titanium in comparison with β-matrix; this effect is known as element partitioning.

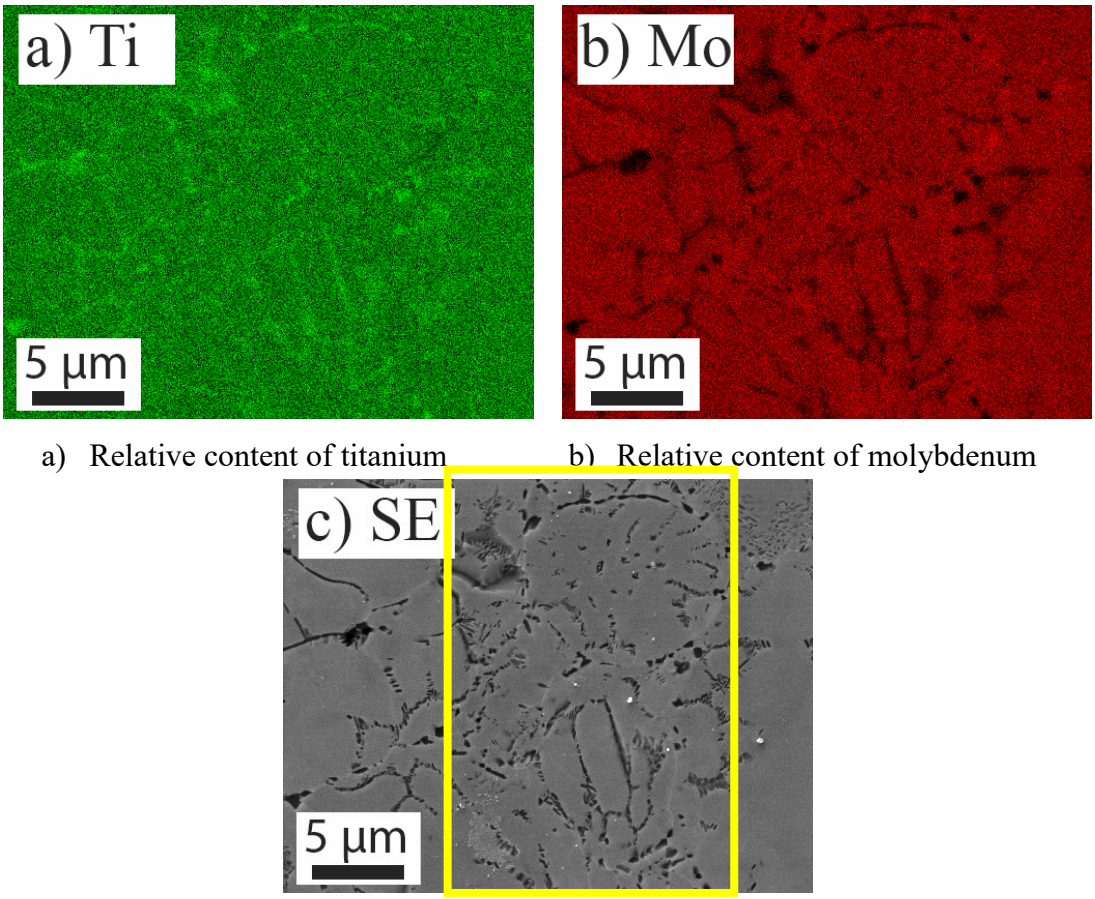

a) Relative content of titanium b) Relative content of molybdenum

c) SE micrograph

Figure 5.10: EDX map of sample i750/3 – a) titanium, b) molybdenum, c) SE micrograph

5.2.2 Microstructure of sintered milled powders

5.2.2.1 SEM imaging

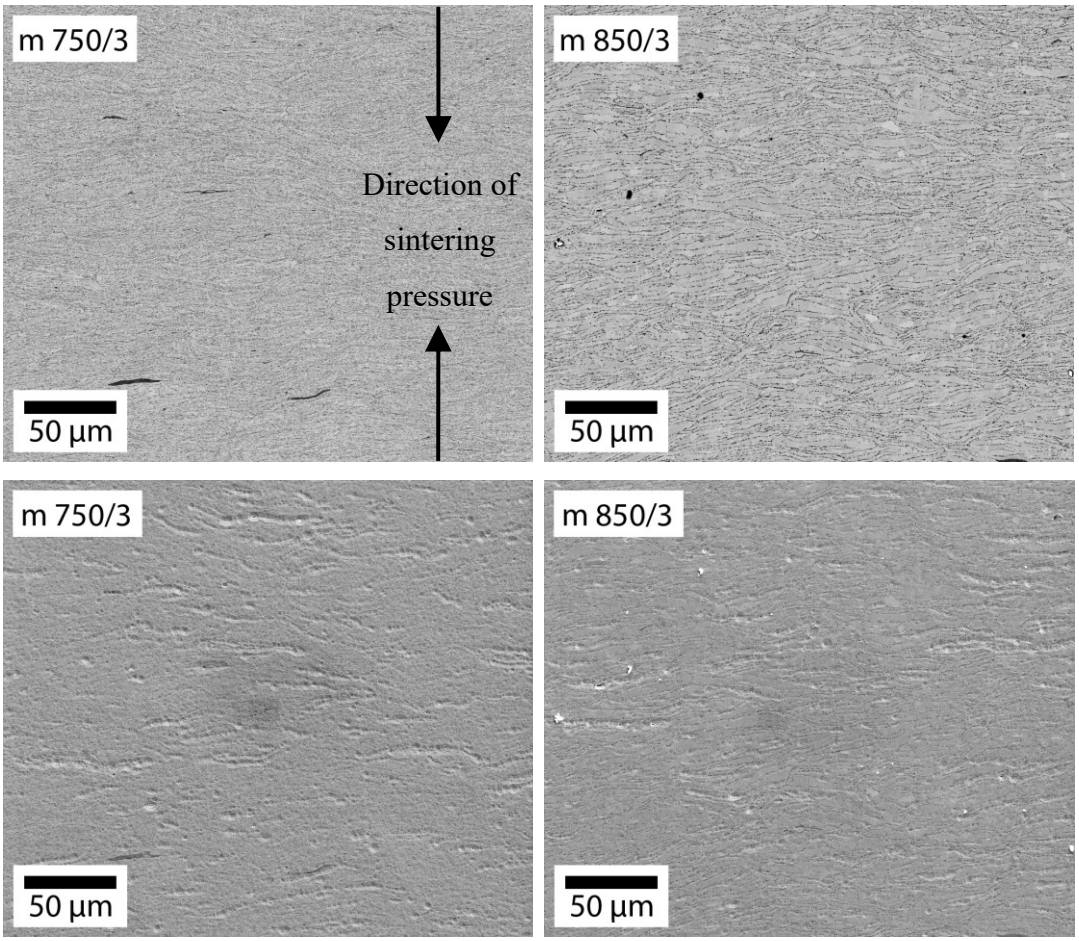

Figure 5.11: Overview of milled powder sintered at 750 °C (left) and at 850 °C (right) for 3 minutes captured (BSE – top and SE – bottom)

In Figure 5.11, the overview micrographs of milled powder sintered at 750 °C for 3 minutes (left) and at 850 °C for 3 minutes (right) is shown. In BSE micrographs, the small black dots are α-phase particles. The elongated black areas in sample sintered at 750 °C are probably powder particles of pure titanium. These few Ti particles contaminated the Ti-15Mo powder during cryo-milling as pure titanium was previously milled in the same mill tank. From the SE micrographs, it is clear that there are no pores in the samples sintered from milled powder. Bulk material with negligible porosity is achieved already after sintering at 750 °C for 3 minutes in the milled powder, contrary to its initial counterpart. Note that α-phase particles are organized in layers, which are not isotropic, but horizontal orientation prevails.

Powder particles after milling are flat (see Figure 5.1), which causes their predominantly horizontal arrangement in the graphite die during sintering [65]. Horizontal alignment of α-phase precipitates may be explained by the assumption that α-phase precipitates grow preferably on the surface of powder particles, as discussed below. Dimples from ion polishing are also seen in the samples sintered from milled powder. These samples must have been prepared by ion polishing to resolve the microstructure in BSE images. Dimples seen in SE images are therefore only remnants from specimen preparation.

Detailed BSE SEM micrographs of the sintered milled powder are shown in Figure 5.12. With increasing sintering time and temperature, the fraction of α-phase decreases while the size of α-phase particles increases.

The amount of α-phase is significantly higher in comparison with samples sintered from the initial powder. Initial powder sintered at 850 °C for 3 minutes contains very limited amount of α-phase while milled powder always contains significant amount of α-phase independently of sintering conditions.

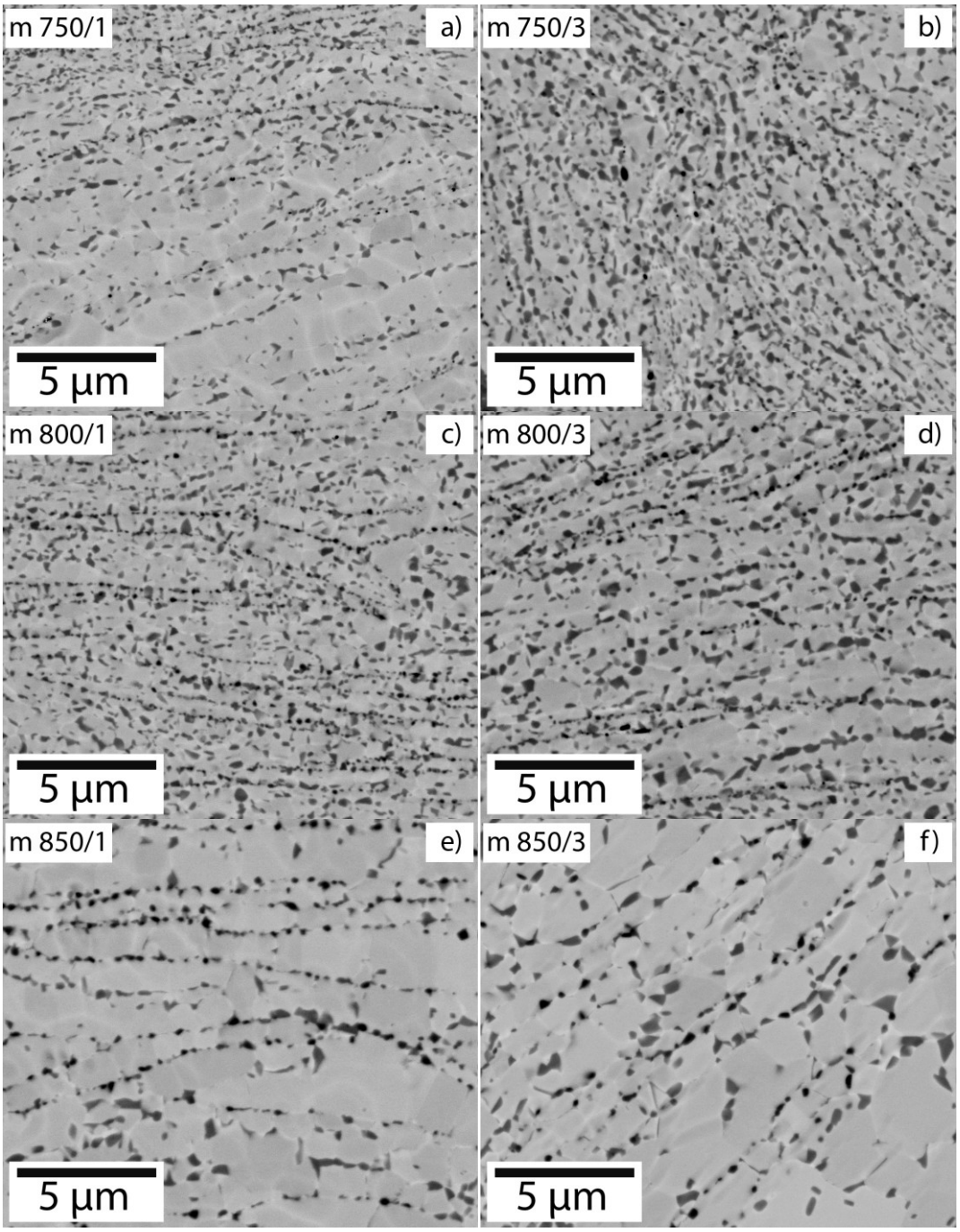

Figure 5.12: SEM micrographs (BSE) of milled samples sintered at 750 °C (top), 800 °C (middle) and 850 °C (bottom) for 1 (left) and 3 (right) minutes

5.2.2.2 Microstructural observation by TKD

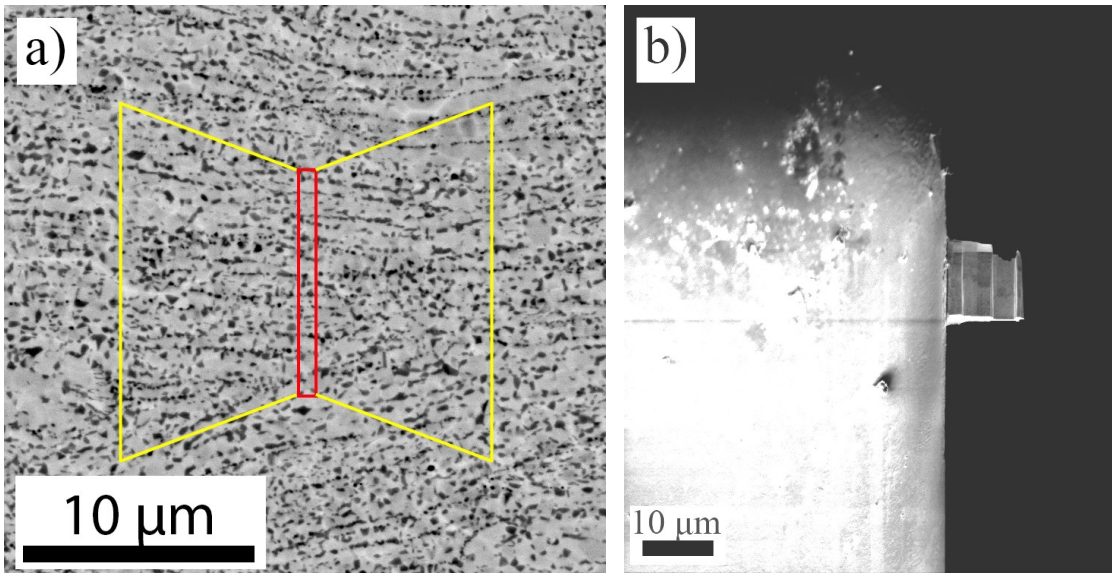

a) A position of lamella on the sample (BSE) b) The lamella placed on a grid (SE)

Figure 5.13: Lamella prepared from sample m750/3, a) A position of lamella on the sample, b) The lamella placed on a grid

Lamella from the sample m750/3 was cut by FIB and investigated by TKD. The position of lamella is shown in Figure 5.13 a). Red rectangle indicates the position of the top of the lamella. Considering that surface of SEM sample is vertically oriented, the lamella is also vertical. Yellow trapezoids in Figure 5.13 a) are trenches which must be 'dug' by FIB. The lamella was thinned by FIB, lifted by nanomanipulator and placed on a grid as shown in Figure 5.13 b). The resulting IPF map of both α and β-phases is shown in Figure 5.14. The non-indexed points are not shown and SE image of the lamella is shown in the background of the IPF map. Figures 5.15 a) and b) show IPF map separately for α phase and β-phase. The phase map is shown in Figure 5.15 c). The size of α-phase particles is in range from tens to hundreds of nanometres, while the size of β-grains is around 1 µm.

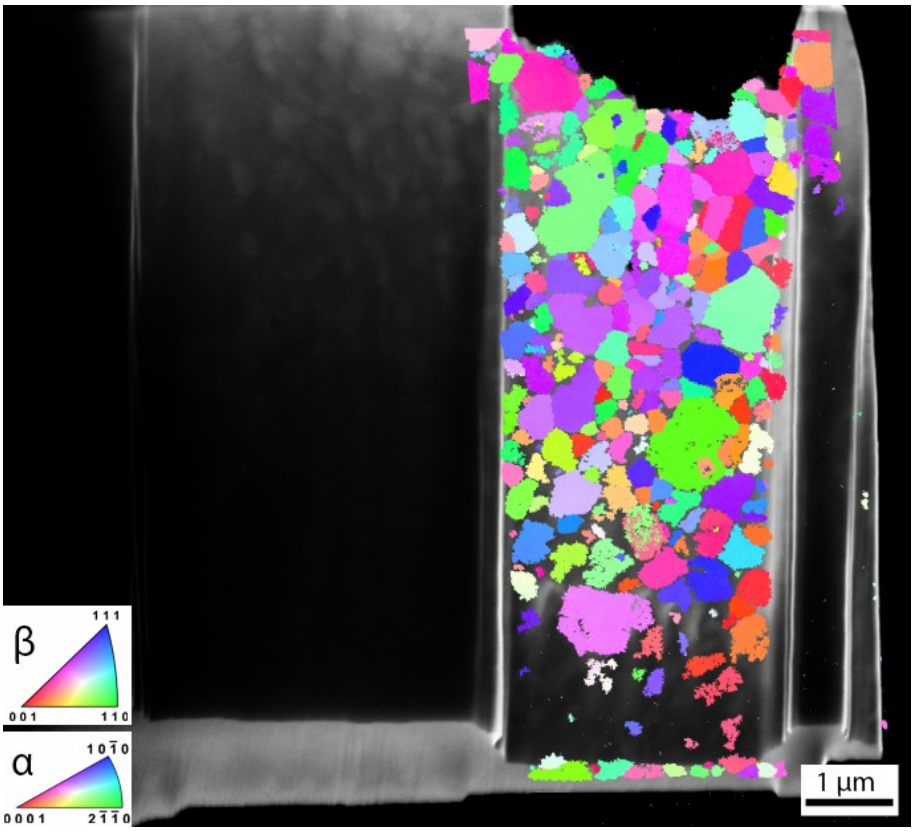

Figure 5.14: TKD IPF map of sample m750/3 overlaid on the SE image of the lamella

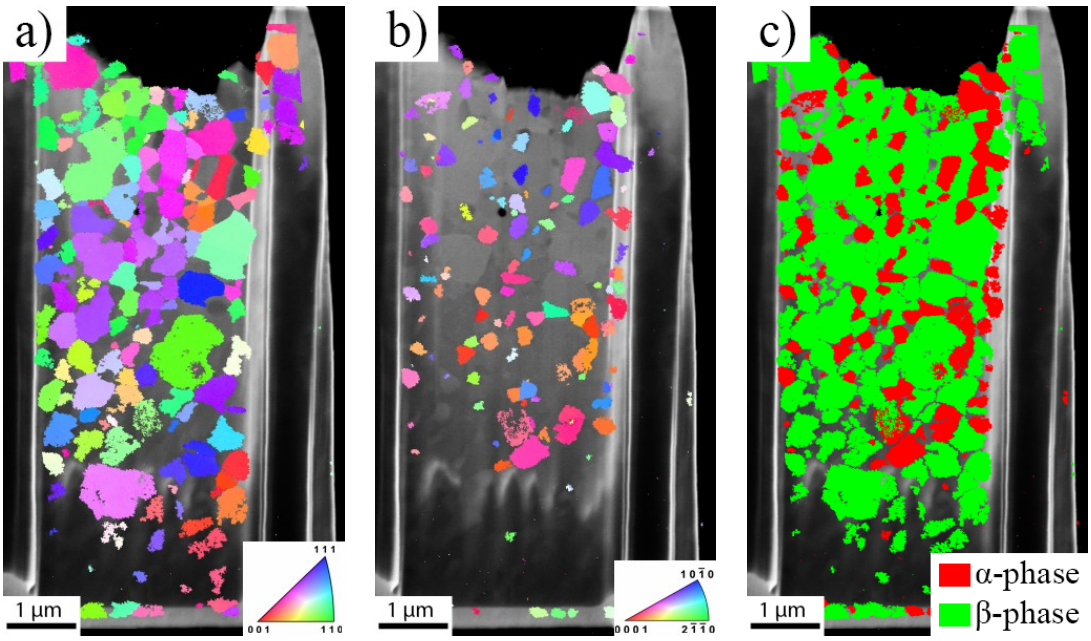

a) β-phase b) α-phase c) phase map

Figure 5.15: TKD maps of sample m750/3 overlaid on the SE image of the lamella, a) IPF map of β-phase, b) IPF map of α-phase, c) phase map

5.2.3 Phase composition measured by XRD

The phase composition was studied by powder XRD. An example of the XRD pattern for i750/1 sample is displayed in Figure 5.16, in which measured data (black) and the fitted curve (red) are displayed as well as their difference (blue). The intensity is displayed in logarithmic scale in order to accentuate small peaks of evolving α and ω-phases.

The measured patterns could not be accurately fitted by the Rietveld approach due to a strong texture; therefore volume fraction of each phase could not be determined. However, it is possible to compare qualitatively the phase composition of different conditions.

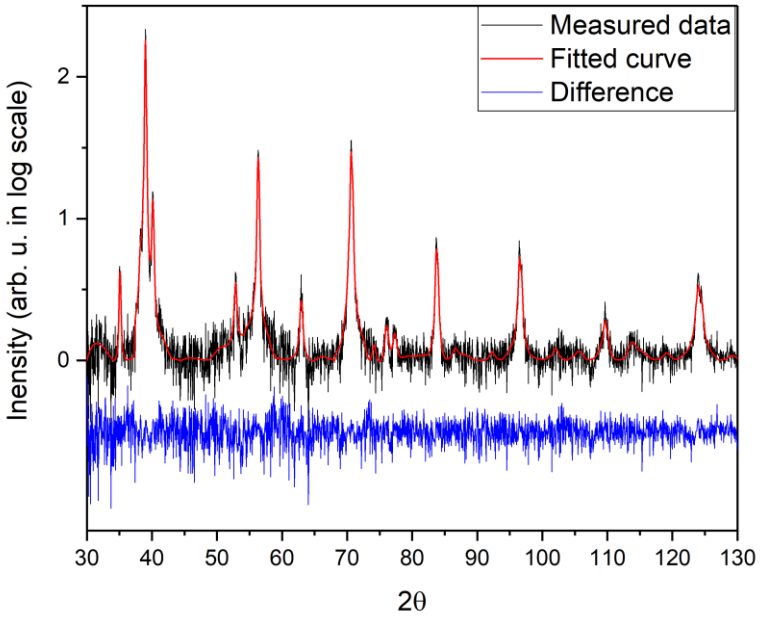

Figure 5.16: XRD-pattern of initial powder sintered at 750 °C for 1 minute – comparison of measured data with the fitted curve.

XRD-patterns of the initial powder and bulk samples sintered from initial powder at selected sintering conditions are shown in Figure 5.17. Small ω-peaks can be identified at $2\theta \approx 32°, 45°$ and $80°$ (see white arrows). Peaks are very wide due to the small size of ω-phase particles. Pattern measured for sample sintered at 850 °C for 3 minutes (i850/3) shows the mixture of β and ω-phases while the α-phase was not identified (as the volume fraction of α-phase is below detection limit. This is

consistent with SEM observations and is caused by sintering at temperature well above the β-transus temperature. Samples sintered at 800 °C and 750 °C contain α-phase as observed at angles $2\theta \approx 35°$ or $53°$ (see black arrows). ω-phase is present in all samples sintered from initial powder. However, the quantitative analysis is not possible.

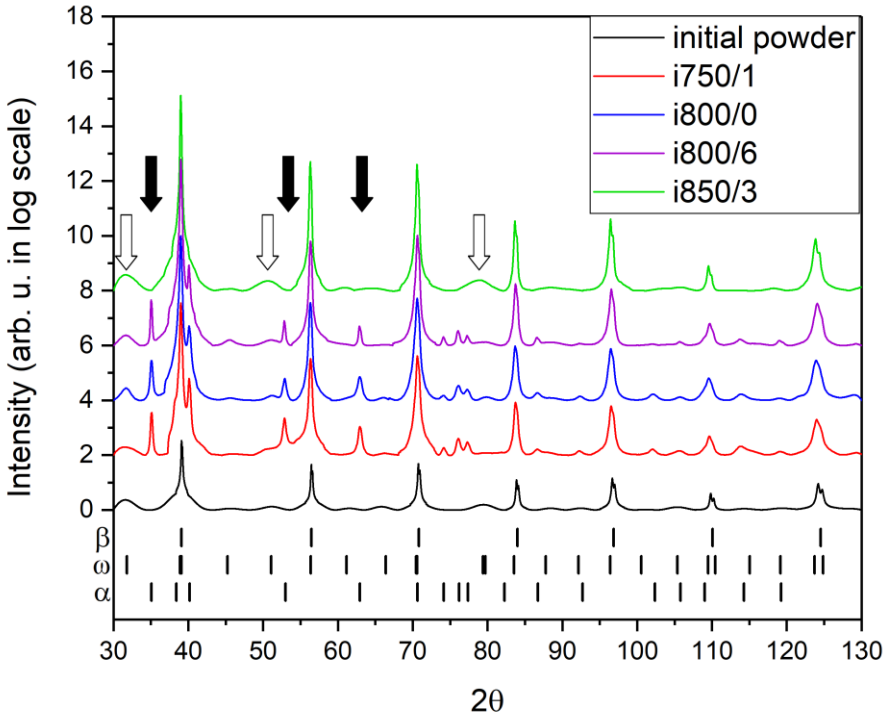

Figure 5.17: XRD-patterns of the initial powder and of the bulk material sintered from the initial powder. The patterns are vertically shifted for clarity.

XRD-patterns of milled powder and bulk samples sintered from milled powder at the same sintering conditions are displayed in Figure 5.18. In the milled powder, peaks of α and β-phase are observed. Peaks are significantly broadened due to high induced deformation. The possible presence of ω-phase in the milled powder cannot be resolved from the pattern since broad ω-peaks could not be distinguished from broad β-peaks.

The material recovers and recrystallizes during sintering and the peak broadening is significantly reduced. All samples sintered from the milled powder contain

significant amount of α-phase which is again consistent with SEM observations. The presence of ω-phase is ambiguous in samples sintered from milled powder.

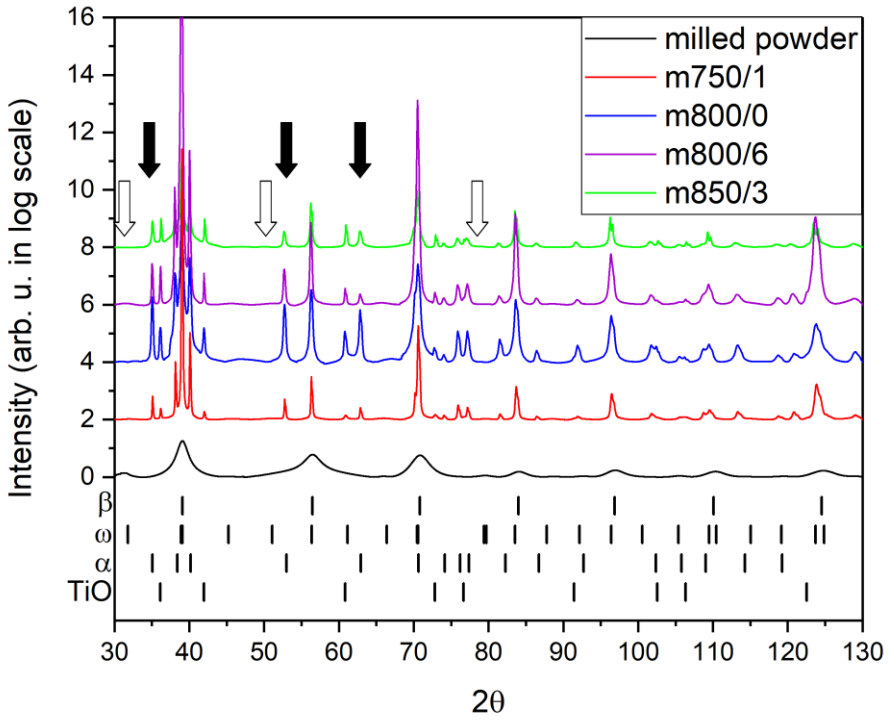

Figure 5.18: XRD-patterns of the milled powder and of the bulk material sintered from the milled powder. The patterns are vertically shifted for clarity.

5.2.4 Chemical contamination measured by CGHE

Contamination of selected sintered samples by oxygen, hydrogen and nitrogen was measured by CGHE and the results are shown in Table 5.2. The results from Table 5.1 are repeated in Table 5.2 for easier comparison. The contamination of sintered milled powders is significantly higher than that of sintered initial powders. It is consistent with the results for powders in Table 5.1. The change in contamination by nitrogen during sintering is negligible, but contamination by oxygen and hydrogen of the initial powder increases after sintering. Conversely, the contamination of the milled powder decreases after sintering. Due to milling in the presence of stearic acid, powder particles are covered by a thin film of stearic acid preventing cold-welding. During sintering, the stearic acid is partly decomposed and

the products are removed by heating in vacuum. The temperature of sintering does not have a significant effect on contamination.

Table 5.2: Chemical contamination of chosen samples

Sample	Oxygen	Hydrogen	Nitrogen
Initial powder	0.198	<0.001	0.014
Milled powder	0.784	0.147	0.030
i750/3	0.267	0.026	0.018
i850/3	0.246	0.028	0.017
m750/3	0.572	0.085	0.028
m850/3	0.601	0.088	0.025

5.2.5 Mechanical properties

5.2.5.1 Microhardness measurements

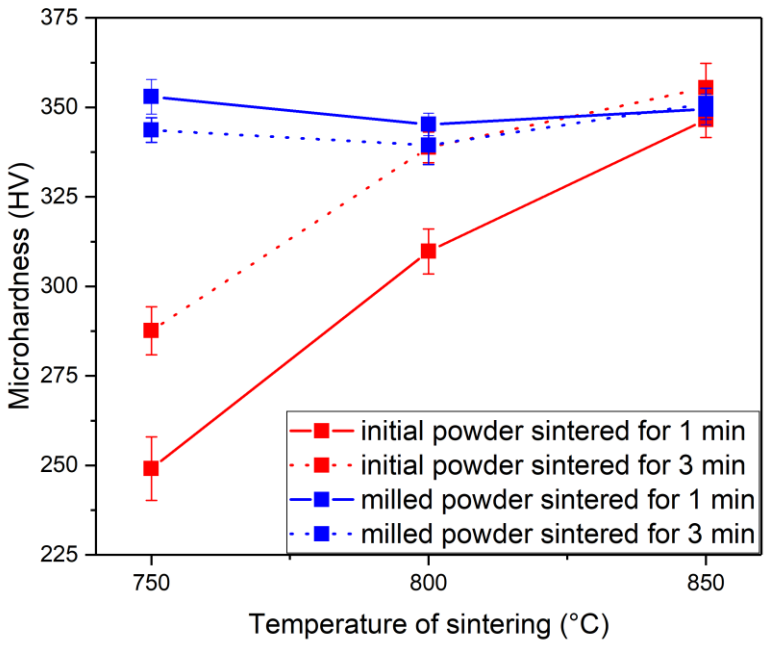

Figure 5.19: Dependence of microhardness on the temperature of non-milled and milled samples for different times of sintering

The dependence of microhardness on the temperature and time of sintering of the initial and milled material is shown in Figure 5.19. For initial samples the

microhardness increases with increasing temperature and sintering time due to reduced porosity. In the case of milled samples, the microhardness is almost constant for all investigated sintering temperatures and times. This indicates that the material is already well compacted when sintering at 750 °C for 1 minute.

5.2.5.2 Tensile tests

The true-stress – true-plastic-strain flow curves for selected conditions are shown in Figure 5.20. Two specimens per condition were measured. Milled powder sintered at 850 °C for 3 minutes cracked at the elastic part of stress-strain curve and is not shown in the figure.

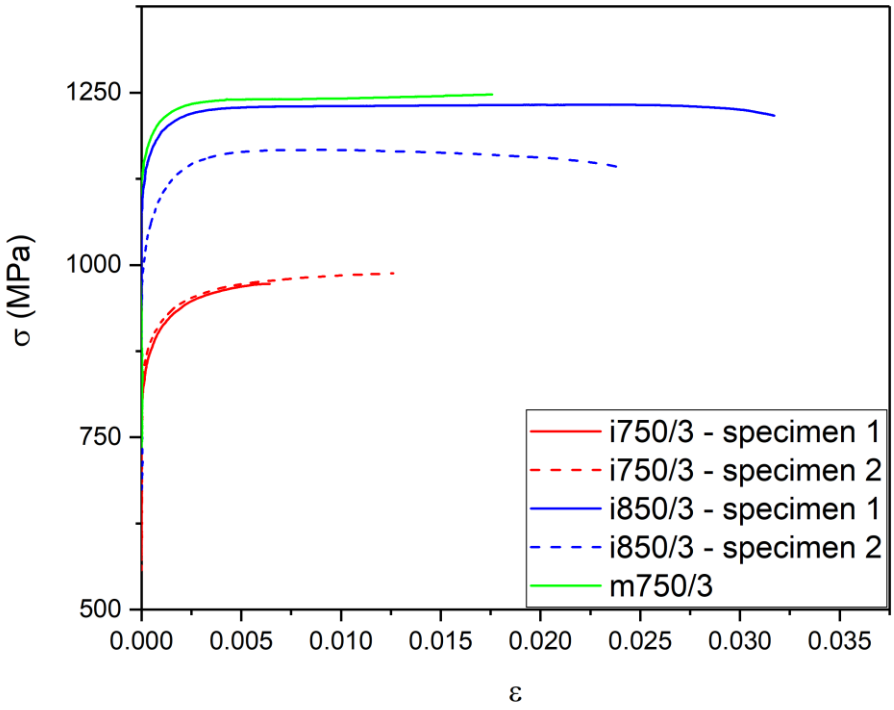

Figure 5.20: Tensile tests: true stress – true strain curves for chosen sintered samples

The yield strength of initial powder sintered at 850 °C is significanlty higher than the yield strength of initial powder sintered at 750 °C. Milled powder sintered at 750 °C has comparable yield strength as the initial sample sintered at 850 °C. However, tensile tests of milled materials were not successful due to small dimensions of testing samples (explained in chapter 6.2.3.2). The ductility of all samples is very low. Note that the sample m850/3 failed already during elastic deformation.

5.2.5.3 Compression tests

True stress – true strain compression flow curves for chosen sintered samples are shown in Figure 5.21. Two specimens were tested per condition with almost equivalent results; therefore only one flow curve per condition is shown. The yield stress increases with increasing sintering temperature for initial powders which correlates with the decreasing porosity. The yield stress of milled powder is independent of the temperature of sintering.

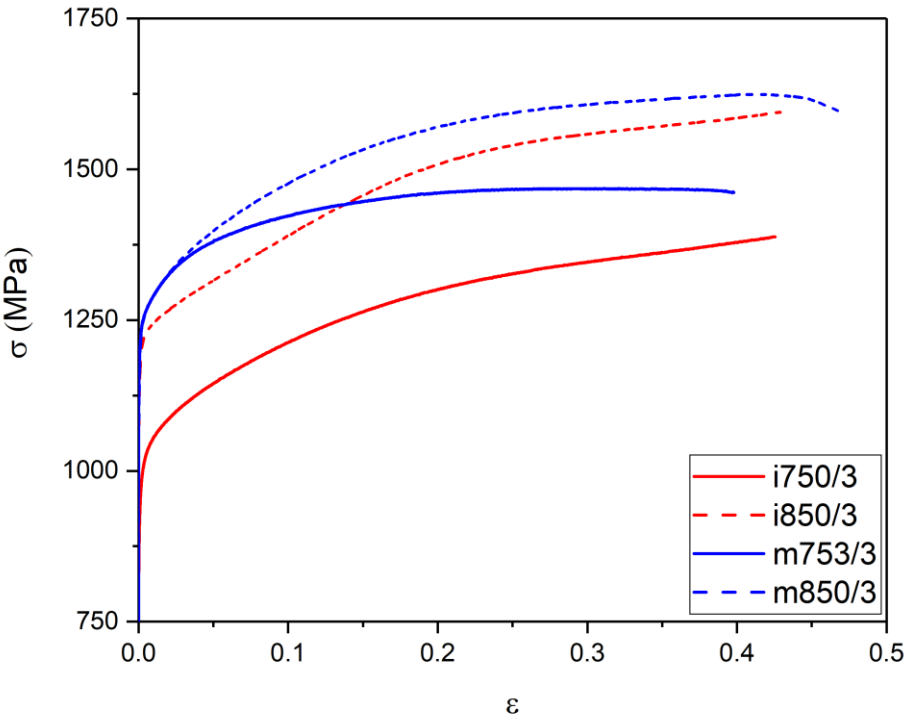

Figure 5.21: Compression tests: true stress – true strain curves for selected sintered samples

6 Discussion

6.1 Cryogenic milling

Gas atomization of Ti-15Mo alloy resulted in spherical powder particles with the size in range from units of micrometres up to 30 μm. The distribution of molybdenum within the powder particles is inhomogeneous (see Figure 5.3).

Significant refinement of microstructure of powder after milling can be indirectly inferred from the broadening of XRD peaks. The refinement is caused by repetitive plastic deformation during milling similarly to Ti [37]. The process of cryogenic milling can be compared with SPD processes. The grain size of around 200 nm was reached after deformation of Ti-15Mo by HPT [29, 30, 66]. Ultra-fine grained microstructure of commercially pure titanium with grain size around 100 nm was reached [37] by cryogenic milling.

The contamination of the powder by oxygen, hydrogen and nitrogen increased after milling even if it was performed in liquid argon. It may be caused by the addition of the process control agent – the stearic acid – which contains hydrogen and oxygen. It can be calculated that stearic acid can cause an increase of amount of oxygen by 0.113 wt% and of hydrogen of 0.127 wt%. Measured hydrogen content presented in Table 5.1 is reasonably consistent with this calculation, but the content of oxygen is significantly higher. Additional contamination by oxygen may be caused by oxidation of powder particles surface during milling because the used liquid argon was not ultra-pure. Note that total surface area is significantly higher in the milled powder due to disc-shaped particles.

6.2 Spark plasma sintering of initial and milled powder

6.2.1 Compaction

Low temperatures and times are not sufficient for sintering the initial powder while the same conditions are sufficient for sintering the milled one, as shown by SEM. It may have several reasons. First, the shape of powder particles significantly affects the compaction. Sintering occurs at points of contact of the neighbouring particles [44]. The disc-shaped particles (milled powder) are mutually in closer

contact when compared to the ball-shaped particles (initial powder). This results in enhanced compaction. Moreover, diffusion lengths required for full sintering of thin flat particles are significantly shorter than for ball particles with comparable average particle volume. Another important fact is a large strain imposed to the milled powder. Increased concentration of defects causes the enhanced diffusivity [20] and therefore the compaction is also enhanced.

As shown in Figure 5.9, the residual porosity of sintered initial powder also changes with the distance from the centre of the cylindrical sample. It grows from the centre of the sample to the periphery of the cylinder, but it does not change along the cylinder axis. This result corresponds to modelling of temperature distribution within cylindrical sample during sintering as reported in [67]. The modelling shows that the temperature dependence on the distance from axis of the cylinder has a Gaussian shape with a maximum in the centre of the specimen. The difference in porosity of the central part and the periphery part decreases with increasing sintering time. While the difference is significant for the sample i800/0, it is not practically observed for samples i800/3 and i800/6 since negligible porosity is achieved everywhere in the sample after longer sintering at 800 °C.

There is no difference in porosity of central part and periphery part of sintered milled powders samples because of the generally lower porosity. Inhomogeneity of milled Ti powder was observed after sintering at lower temperatures and times [68].

6.2.2 Phase composition

The β-transus temperature of Ti-15Mo alloy is 774±14 °C [21] and therefore α-phase precipitates during sintering at 750 °C. However, samples sintered from initial powder at 800 °C and 850 °C also contain some amount of α-phase. As observed in Figure 5.3, material after gas atomization is not chemically homogeneous. In Mo depleted areas, the true β-transus might be significantly higher and α-phase might be formed during sintering. Another possibility is the precipitation of α-phase during cooling. Cooling rate after sintering at 850 °C can be inferred from Figure 4.1. It follows that the total time spent in range of temperatures 750 °C – 500 °C [17, 18], which is critical for α-phase precipitation, is about 1-2 minutes. This time period

might be sufficient for precipitation of α-particles at grain boundaries where both their nucleation and growth are enhanced [69].

Samples sintered from the milled powder contain significantly more α-phase in comparison with the initial powder sintered at the same conditions. It can be seen for instance in samples sintered at 850 °C for 3 minutes (see Figures 5.8 and 5.12). While this condition prepared from initial powder contains only limited amount of α-phase, the same specimen sintered from the milled powder contains a substantial amount α-phase particles. This may be caused by increased temperature of β-transus due to contamination by oxygen [70, 71]. The contamination of milled powder and sintered samples manufactured from the milled powder is much higher than the contamination of the initial powder counterparts as shown in Table 5.2. The temperature of β-transus may exceed the sintering temperature of 850 °C and α-phase may precipitate during sintering. Several studies reported that α-phase precipitation is significantly enhanced in severely deformed and ultra-fine grained materials due to higher diffusion rate caused by high concentration of defects [72–75]. Similar effect can be expected in the deformed milled powder resulting in substantial α-phase precipitation.

In [55], the Ti-Mo alloys with different Mo content up to 14 wt% were sintered from elemental powder of 99.9 % purity. It is shown that with increasing Mo content the β-phase is more stabilized and the amount of α-phase decreases. In Ti-14Mo alloy, α-phase precipitates only at grain boundaries. This result is well comparable to Ti-15Mo alloy sintered at 850 °C for 3 minutes with the low content of α-phase present only at particle interfaces (see Figure 5.8).

Material after sintering may also contain ω_{iso}-phase stabilized by diffusion during cooling. During cooling the specimen is exposed to the temperatures of 450 °C – 250 °C for about 3-4 minutes which is critical for ω-phase formation [76]. ω-phase formation during cooling is, however, affected by the presence of α-phase particles. During α-phase precipitation element partitioning occurs as proved by EDS mapping in Figure 5.10. α-phase displaces β-stabilizing molybdenum and the β-matrix becomes more β-stabilized – chemical composition of surrounding β-matrix efficiently moves to the right in the phase diagram in Figure 1.4. Due to this fact, ω-phase formation is suppressed. Samples with higher amount of α-phase have

therefore generally lower amount of ω-phase. Lower content of ω-phase in samples sintered from the milled powder (i.e. samples containing substantial amount of α-phase) was generally confirmed by XRD-measurements.

Mechanical alloying of Ti-35Nb-7Zr-5Ta (TNTZ) alloy reported in [56] induced high deformation similarly to cryogenic milling. After SPS the phase composition and microstructure were similar to our observations despite studied alloy TNTZ is generally more β-stabilized. Although the used sintering temperatures 950 °C – 1150 °C are well above temperature of β-transus of the alloy, all samples contain the duplex α+β-microstructure. It can be caused by insufficient cooling rate (not reported) or by enhanced temperature of β-transus due to chemical contamination. The contamination by oxygen is lower, while the contamination by nitrogen and iron is significantly higher in comparison to our results, which is caused by the nature of mechanical alloying at room temperature in a planetary mill without PCA.

6.2.3 Mechanical properties

6.2.3.1 Microhardness

Microhardness of samples sintered from initial powder increases with both time and temperature of sintering which is attributed to the decrease of porosity [77]. On the other hand, microhardness of samples sintered from the milled powder is constant. The porosity does not play an important role because these samples are well-compacted already after short sintering times at low temperatures. High microhardness of the samples sintered from milled powder can be caused by: microstructural refinement, the contamination by oxygen or the presence of fine structure of α-phase precipitates. Milled powder sintered at 750 °C is strengthened by fine-grained microstructure (grain size below 1 μm). However, the grain size increases with increasing temperature of sintering. α-phase strengthens the material by precipitation hardening. However, the fraction of α-phase decreases with increasing sintering temperature and the α-phase particles are coarser and the effect of precipitation hardening is therefore lower. Contamination by oxygen is substantial (see Table 5.2) and may constitute the dominant strengthening mechanism.

Another important factor affecting mechanical properties is ω-phase which strengthen the material by dispersion hardening. As it is described above (in chapter

6.6.2), material with lower amount of α-phase is more prone to the ω-phase formation. Excessive formation of ω-phase may cause strengthening of sintered initial powder. This may explain rather surprising result that the microhardness of initial powder compacted at 850 °C is the same as the microhardness of sintered milled powder. Similarly, enhanced fraction of ω-phase in milled powder sintered at higher temperature of 850 °C (when compared to milled powder sintered at lower temperatures) may compensate growth of β-grains and α-precipitates in terms of hardness.

The maximum microhardness reached is about 350 HV what is comparable to the microhardness of Ti-15Mo alloy in aged condition prepared by standard methods [31]. Microhardness of severely Ti-15Mo can be as high as 500 HV [29].

6.2.3.2 Deformation tests

Initial powder sintered at 750 °C has lower yield strength in comparison with initial powder sintered at 850 °C due to its higher porosity.

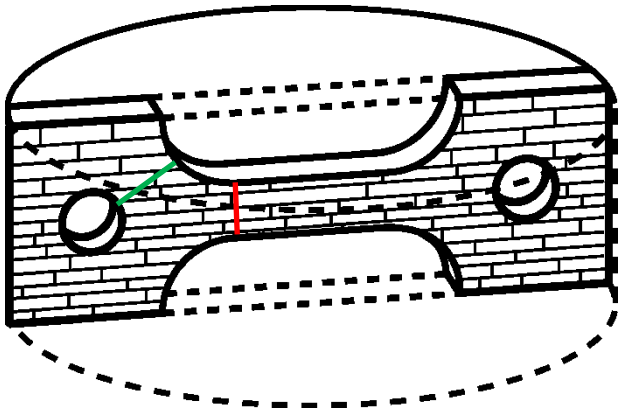

Figure 6.1: The position of the tensile specimen within the sample with a scheme of layers of milled powder particles inside the sample.

The tensile tests of sintered milled powder were not successful probably due to small dimensions of tensile samples and their design. The position of tensile specimen in the sintered sample is schematically shown in Figure 6.1. The tensile specimen was too small and the cross section of the gauge part (red line in Figure 6.1) had to be therefore only slightly smaller than the cross section between the edge of the sample and a hole made for sample fixing (the green line in Figure 6.1) The results are

therefore affected by the quality of the specimen surface and sample may fail out of the gauge part.

Furthermore, the measurement of the sintered milled powder is affected by the direction of deformation with respect of the powder particle layers. The direction of deformation lies in a plane of powder particle layers (see Figure 6.1). During deformation, the sample is also strained around the holding holes. The stress in this area causes a delamination of powder particle layers and milled samples tend to fail around the hole instead in the gauge part. Samples after tensile deformation are shown in Figure 6.2.

Moreover, high oxygen content in the milled powder may also negatively affect the ductility causing the embrittlement of α-phase and consequently the embrittlement of the material as a whole.

Figure 6.2: A photo of tensile samples after the test

Conclusions

The gas atomized Ti-15Mo powder was successfully cryogenically milled and subsequently spark plasma sintered at temperatures in range of 750-850 °C for different sintering times in the range of 0-6 minutes. The morphology of both initial and milled powders was observed by SEM. Microstructure of the sintered samples was investigated by SEM, EBSD, EDX and TKD. Contamination of samples by oxygen, hydrogen and nitrogen was measured by CGHE and phase composition by XRD. Mechanical properties were determined and the effect of contamination, microstructure and phase composition was discussed.

- During cryogenic milling, the shape of gas atomized Ti-15Mo powder particles changed from spherical to disc-shaped.
- The contamination of powder by hydrogen, nitrogen and oxygen is higher after milling which is caused by the addition of the stearic acid as the process control agent and by contamination from the cooling liquid.
- The milled powder is well compacted already after sintering at 750 °C for 1 minute while higher temperature or significantly longer sintering times are necessary for compaction of initial powders.
- After sintering of the initial powder for short sintering times, the porosity in the central part of the sample is lower than the porosity in periphery part of sample. It is consistent with the temperature distribution.
- Sintering of both initial and milled powders resulted in the formation of α+β-structure. However, the content of α-phase is significantly higher in the samples sintered from milled powder.
- Increased precipitation of α-phase during sintering of the milled powder is caused by a higher contamination by α-stabilizing oxygen and by refined microstructure which promotes the nucleation of α-phase precipitates.
- The evolution of microhardness is affected by the residual porosity, the phase composition and the contamination by oxygen.
- The compression tests showed an increasing strength of the material sintered at longer times.

Bibliography

[1] LEYENS, C. and M. PETERS. *Titanium and titanium alloys*. B.m.: Wiley-VCH., 2003.

[2] LÜTJERING, G. and J.C. WILLIAMS. *Titanium*. Berlin: Springer-Verlag, 2003.

[3] DE FONTAINE, D. Simple models for the omega phase transformation. *Metallurgical Transactions A*. 1988, vol. 19, no. 2, pp. 169–175. 10.1007/BF02652523

[4] SANATI, M., D. WEST and R. ALBERS. First-principles study of ω-phase formation in the Ti3Al2V system. *Journal of Physics: Condensed Matter*. 2007, vol. 19, p. 386221. 10.1088/0953-8984/19/38/386221

[5] SIKKA, S.K., Y.K. VOHRA and R. CHIDAMBARAM. Omega phase in materials. *Progress in Materials Science*. 1982, vol. 27, no. 3, p. 245. 10.1016/0079-6425(82)90002-0

[6] DUERIG, T.W., G.T. TERLINDE and J.C. WILLIAMS. *The Omega-Phase Reaction in Titanium Alloys.* JWTR-6. B.m.: CARNEGIE-MELLON UNIV PITTSBURGH PA DEPT OF METALLURGY AND MATERIALS SCIENCE. 1980 [accessed. 27. January 2019]. Retrieved from: https://apps.dtic.mil/docs/citations/ADA093964

[7] WILLIAMS, J.C. *Critical review: kinetics and phase transformations*. B.m.: Titanium science and technology, 1973.

[8] LÜTJERING, G. and J.C. WILLIAMS. *Titanium*. Berlin: Springer-Verlag, 2003.

[9] DE FONTAINE, D., N.E. PATON and J.C. WILLIAMS. The omega phase transformation in titanium alloys as an example of displacement controlled reactions. *Acta Metallurgica*. 1971, vol. 19, no. 11, pp. 1153–1162. 10.1016/0001-6160(71)90047-2

[10] FURUHARA, T., T. MAKINO, Y. IDEI, H. ISHIGAKI, A. TAKADA and T. MAKI. Morphology and Crystallography of α Precipitates in β Ti–Mo Binary Alloys. *Materials Transactions, JIM*. 1998, vol. 39, no. 1, pp. 31–39. 10.2320/matertrans1989.39.31

[11] DUERIG, T.W., G.T. TERLINDE and J.C. WILLIAMS. Phase transformations and tensile properties of Ti-10V-2Fe-3AI. *Metallurgical Transactions A*. 1980, vol. 11, no. 12, pp. 1987–1998. 10.1007/BF02655118

[12] ZHÁŇAL, P. *Master thesis: Study of phase transformations in Ti alloys*. B.m.: Charles University in Prague, 2014.

[13] WILLIAMS, J.C. and M.J. BLACKBURN. THE INFLUENCE OF MISFIT ON THE MORPHOLOGY AND STABILITY OF THE OMEGA PHASE IN TITANIUM--TRANSITION METAL ALLOYS. *Trans. Met. Soc. AIME, 245: 2352-5(Oct. 1969).* 1969, vol. 245.

[14] AZIMZADEH, S. and H.J. RACK. Phase transformations in Ti-6.8Mo-4.5Fe-1.5Al. *Metallurgical and Materials Transactions A*. 1998, vol. 29, no. 10, pp. 2455–2467. 10.1007/s11661-998-0217-8

[15] Properties: Titanium Alloys - Ti6Al7Nb Properties and Applications. *AZoM.com*. [accessed. 9. May 2019]. Retrieved from: https://www.azom.com/properties.aspx?ArticleID=2064

[16] DISEGI, J. *Implant Materials. Wrought Titanium -15% Molybdenum*. B.m.: Synthes, 2009.

[17] ZHÁŇAL, P., P. HARCUBA, M. HÁJEK, B. SMOLA, J. STRÁSKÝ, J. ŠMILAUEROVÁ, J. VESELÝ and M. JANEČEK. Evolution of ω phase during heating of metastable β titanium alloy Ti–15Mo. *Journal of Materials Science*. 2018, vol. 53, no. 1, pp. 837–845. 10.1007/s10853-017-1519-2

[18] ZHÁŇAL, P., P. HARCUBA, J. ŠMILAUEROVÁ, J. STRÁSKÝ, M. JANEČEK, B. SMOLA and M. HÁJEK. Phase Transformations in Ti-15Mo Investigated by in situ Electrical Resistance. *Acta Physica Polonica A*. 2015, vol. 128, no. 4, pp. 779–782. 10.12693/APhysPolA.128.779

[19] BARTHA, K., A. TERYNKOVÁ, J. STRÁSKÝ, P. MINÁRIK, J. VESELÝ, V. POLYAKOVA, I. SEMENOVA and M. JANEČEK. Inhomogeneous Precipitation of the α-Phase in Ti15Mo Alloy Deformed by ECAP. *Trans Tech Publication*. 2018, no. 941, pp. 1183–1188. 10.4028/www.scientific.net/MSF.941.1183

[20] BARTHA, K., J. STRÁSKÝ, P. HARCUBA, I. SEMENOVA, V. POLYAKOVA and M. JANEČEK. Heterogeneous Precipitation of the α-Phase in Ti15Mo Alloy Subjected to High Pressure Torsion. *ACTA PHYSICA POLONICA A*. 2018, no. 134, pp. 790–793. 10.12693/APhysPolA.134.790

[21] *ATI 15Mo^{TM}*. [accessed. 10. May 2019]. Retrieved from: https://www.atimetals.com/Products/Pages/ati-ti-15mo.aspx

[22] LANGDON, T.G. Twenty-five years of ultrafine-grained materials: Achieving exceptional properties through grain refinement. *Acta Materialia*. 2013, vol. 61, no. 19, pp. 7035–7059. 10.1016/j.actamat.2013.08.018

[23] SYLWESTROWICZ, W. and E.O. HALL. The Deformation and Ageing of Mild Steel. *Proceedings of the Physical Society. Section B*. 1951, vol. 64, no. 6, p. 495. 10.1088/0370-1301/64/6/305

[24] PETCH, N.J. The cleavage strength of polycrystals. 1953, vol. 174, pp. 25–28.

[25] ZHU, Y.T., T.C. LOWE and T.G. LANGDON. Performance and applications of nanostructured materials produced by severe plastic deformation. *Scripta Materialia*. 2004, vol. 51, no. 8, Viewpoint set no. 35. Metals and alloys with a structural scale from the micrometer to the atomic dimensions, pp. 825–830. 10.1016/j.scriptamat.2004.05.006

[26] VALIEV, R.Z., Y. ESTRIN, Z. HORITA, T.G. LANGDON, M.J. ZECHETBAUER and Y.T. ZHU. Producing bulk ultrafine-grained materials by severe plastic deformation. *JOM*. 2006, vol. 58, no. 4, pp. 33–39. 10.1007/s11837-006-0213-7

[27] YILMAZER, H., M. NIINOMI, M. NAKAI, J. HIEDA, Y. TODAKA, T. AKAHORI and T. MIYAZAKI. Heterogeneous structure and mechanical hardness of biomedical β-type Ti–29Nb–13Ta–4.6Zr subjected to high-pressure torsion. *Journal of the Mechanical Behavior of Biomedical Materials*. 2012, vol. 10, pp. 235–245. 10.1016/j.jmbbm.2012.02.022

[28] YILMAZER, H., M. NIINOMI, K. CHO, M. NAKAI, J. HIEDA, S. SATO and Y. TODAKA. Microstructural evolution of precipitation-hardened β-type titanium alloy through high-pressure torsion. *Acta Materialia*. 2014, vol. 80, pp. 172–182. 10.1016/j.actamat.2014.07.041

[29] VÁCLAVOVÁ, K., J. STRÁSKÝ, V. POLYAKOVA, J. STRÁSKÁ, J. NEJEZCHLEBOVÁ, H. SEINER, I. SEMENOVA and M. JANEČEK. Microhardness and microstructure evolution of ultra-fine grained Ti-15Mo and TIMETAL LCB alloys prepared by high pressure torsion. *Materials Science and Engineering: A*. 2017, vol. 682, pp. 220–228. 10.1016/j.msea.2016.11.038

[30] JANEČEK, M., J. ČÍŽEK, J. STRÁSKÝ, K. VÁCLAVOVÁ, P. HRUŠKA, V. POLYAKOVA, S. GATINA and I. SEMENOVA. *Microstructure evolution in solution treated Ti15Mo alloy processed by high pressure torsion*. B.m.: Materials Characterisation, 2014.

[31] VÁCLAVOVÁ, K., J. STRÁSKÝ, J. VESELÝ, S. GATINA, V. POLYAKOVA, I. SEMENOVA and M. JANEČEK. Evolution of Microstructure and Microhardness in Ti-15Mo β-Ti Alloy Prepared by High Pressure Torsion. *Materials Science Forum*. 2016, no. 879, pp. 2555–2560. 10.4028/www.scientific.net/MSF.879.2555

[32] ZHÁŇAL, P., K. VÁCLAVOVÁ, B. HADZIMA, P. HARCUBA, J. STRÁSKÝ, M. JANEČEK, V. POLYAKOVA, I. SEMENOVA, M. HÁJEK and K. HAJIZADEH. Thermal stability of ultrafine-grained commercial purity Ti and Ti–6Al–7Nb alloy investigated by electrical resistance, microhardness and scanning electron microscopy. *Materials Science and Engineering: A*. 2016, vol. C, no. 651, pp. 886–892. 10.1016/j.msea.2015.11.029

[33] QIAN, M. and F.H. FROES. *Titanium Powder Metallurgy*. Amsterdam, The Netherlands: Elsevier, 2015 [accessed. 7. May 2019]. ISBN 978-0-12-800054-0. 10.1016/C2013-0-13619-7

[34] *Welcome to Kaye and Laby Online*. [accessed. 18. February 2019]. Retrieved from: http://www.kayelaby.npl.co.uk/

[35] SURYANARAYANA, C. Mechanical alloying and milling. *Progress in Materials Science*. 2001, vol. 46, no. 1, pp. 1–184. 10.1016/S0079-6425(99)00010-9

[36] KOCH, C.C. Synthesis of nanostructured materials by mechanical milling: problems and opportunities. *Nanostructured Materials*. 1997, vol. 9, no. 1, pp. 13–22. 10.1016/S0965-9773(97)00014-7

[37] KOZLÍK, J., J. STRÁSKÝ, P. HARCUBA, I. IBRAGIMOV, T. CHRÁSKA and M. JANEČEK. Cryogenic Milling of Titanium Powder. *Metals*. 2018, vol. 8, no. 1, p. 31. 10.3390/met8010031

[38] HE, J. and E. LAVERNIA. Development of nanocrystalline structure during cryomilling of Inconel 625. *Journal of Materials Research*. 2001, vol. 16, pp. 2724–2732. 10.1557/JMR.2001.0372

[39] XUN, Y., F.A. MOHAMED and E.J. LAVERNIA. Synthesis of nanocrystalline Zn-22 Pct Al using cryomilling. *Metallurgical and Materials Transactions A*. 2004, vol. 35, no. 2, pp. 573–581. 10.1007/s11661-004-0368-1

[40] ZHOU, F., S.R. NUTT, C.C. BAMPTON and E.J. LAVERNIA. Nanostructure in an Al-Mg-Sc alloy processed by low-energy ball milling at cryogenic temperature. *Metallurgical and Materials Transactions A*. 2003, vol. 34, no. 9, pp. 1985–1992. 10.1007/s11661-003-0163-4

[41] HUTCHINGS, B.P., D.E. CRAWFORD, L. GAO, P. HU and S.L. JAMES. Feedback Kinetics in Mechanochemistry: The Importance of Cohesive States. *Angewandte Chemie*. 2017, vol. 129, no. 48, pp. 15454–15458. 10.1002/ange.201706723

[42] POMMERIN, A., C. WEIDENTHALER, F. SCHÜTH and M. FELDERHOFF. Direct synthesis of pure complex aluminium hydrides by cryomilling. *Scripta Materialia*. 2010, vol. 62, no. 8, pp. 576–578. 10.1016/j.scriptamat.2009.12.041

[43] ERTORER, O., A. ZÚÑIGA, T. TOPPING, W. MOSS and E.J. LAVERNIA. Mechanical Behavior of Cryomilled CP-Ti Consolidated via Quasi-Isostatic Forging. *Metallurgical and Materials Transactions A*. 2008, vol. 40, no. 1, p. 91. 10.1007/s11661-008-9688-x

[44] GUILLON, O., J. GONZALEZ-JULIAN, B. DARGATZ, T. KESSEL, G. SCHIERNING, J. RÄTHEL and M. HERRMANN. Field-Assisted Sintering Technology/Spark Plasma Sintering: Mechanisms, Materials, and Technology Developments. *Advanced Engineering Materials*. 2014, vol. 16, no. 7, pp. 830–849. 10.1002/adem.201300409

[45] YANG, Y.F., S.D. LUO, G.B. SCHAFFER and M. QIAN. Sintering of Ti–10V–2Fe–3Al and mechanical properties. *Materials Science and Engineering: A*. 2011, vol. 528, no. 22, pp. 6719–6726. 10.1016/j.msea.2011.05.041

[46] YANG, Y.F., S.D. LUO, G.B. SCHAFFER and M. QIAN. Impurity scavenging, microstructural refinement and mechanical properties of powder metallurgy titanium and titanium alloys by a small addition of cerium silicide. *Materials Science and Engineering: A*. 2013, vol. 573, pp. 166–174. 10.1016/j.msea.2013.02.042

[47] YANG, Y.F., S.D. LUO and M. QIAN. The effect of lanthanum boride on the sintering, sintered microstructure and mechanical properties of titanium and titanium alloys. *Materials Science and Engineering: A*. 2014, vol. 618, pp. 447–455. 10.1016/j.msea.2014.08.080

[48] YAN, Z., F. CHEN, Y. CAI, J. YIN and Y. ZHENG. Preparation and properties of Ti–4.5Al–6.8Mo–1.5Fe alloy by high-velocity compaction. *Powder Technology*. 2013, vol. 246, pp. 345–350. 10.1016/j.powtec.2013.05.043

[49] GOH, F. c. w, M. a. HODGSON and P. CAO. A New Multifunctional β Ti Alloy Produced via Powder Metallurgy for Biomedical Applications. *International Journal of Modern Physics: Conference Series*. 2012, vol. 06, pp. 688–693. 10.1142/S2010194512003984

[50] RECHTIN, J., E. TORRESANI, E. IVANOV and E. OLEVSKY. Fabrication of Titanium-Niobium-Zirconium-Tantalium Alloy (TNZT) Bioimplant Components with Controllable Porosity by Spark Plasma Sintering. *Materials*. 2018, vol. 11, no. 2. 10.3390/ma11020181

[51] SUN, F., P. ROJAS, A. ZÚÑIGA and E.J. LAVERNIA. Nanostructure in a Ti alloy processed using a cryomilling technique. *Materials Science and Engineering: A*. 2006, vol. 430, no. 1, pp. 90–97. 10.1016/j.msea.2006.05.136

[52] KOZLÍK, J. *Bachelor thesis: Titanium and titanium alloys prepared by cryogenic milling*. B.m.: Univerzita Karlova v Praze, 2016.

[53] CHEN, W. Interdiffusion and atomic mobility in bcc Ti–rich Ti–Nb–Zr system. *Calphad*. 2018, vol. 60, pp. 98–105. 10.1016/j.calphad.2017.12.002

[54] SHARMA, B., S.K. VAJPAI and K. AMEYAMA. Microstructure and properties of beta Ti–Nb alloy prepared by powder metallurgy route using titanium hydride powder. *Journal of Alloys and Compounds*. 2016, vol. 656, pp. 978–986. 10.1016/j.jallcom.2015.10.053

[55] LU, X., B. SUN, T. ZHAO, L. WANG, C. LIU and X. QU. Microstructure and mechanical properties of spark plasma sintered Ti-Mo alloys for dental applications. *International Journal of Minerals, Metallurgy, and Materials*. 2014, vol. 21, no. 5, pp. 479–486. 10.1007/s12613-014-0932-7

[56] ZOU, L.M., C. YANG, Y. LONG, Z.Y. XIAO and Y.Y. LI. Fabrication of biomedical Ti–35Nb–7Zr–5Ta alloys by mechanical alloying and spark plasma sintering. *Powder Metallurgy*. 2012, vol. 55, no. 1, pp. 65–70. 10.1179/1743290111Y.0000000021

[57] LIU, Z. and G. WELSCH. Effects of oxygen and heat treatment on the mechanical properties of alpha and beta titanium alloys. *Metallurgical Transactions A*. 1988, vol. 19, no. 3, pp. 527–542. 10.1007/BF02649267

[58] Kikuchi lines Vs Kikuchi bands (EBSD in SEM). *Physics Forums*. [accessed. 25. February 2019]. Retrieved from: https://www.physicsforums.com/threads/kikuchi-lines-vs-kikuchi-bands-ebsd-in-sem.776916/

[59] KELLER, R.R. and R.H. GEISS. Transmission EBSD from 10 nm domains in a scanning electron microscope. *Journal of Microscopy*. 2012, vol. 245, no. 3, pp. 245–251. 10.1111/j.1365-2818.2011.03566.x

[60] TOKARSKI, T., G. CIOS, A. KULA and P. BAŁA. High quality transmission Kikuchi diffraction analysis of deformed alloys - Case study. *Materials Characterization*. 2016, vol. 121, pp. 231–236. 10.1016/j.matchar.2016.10.013

[61] EDAXBLOG. TRANSMISSION-EBSD – Taking Transparency to a New Level. *EDAX Blog*. 2. October 2014 [accessed. 12. February 2019]. Retrieved from: https://edaxblog.com/2014/10/02/transmisson-ebsd-taking-transparency-to-a-new-level/

[62] KOZLÍK, J. *Master thesis: Microstructure and Texture of Titanium Prepared by Powder Metallurgy*. B.m.: Charles University, 2018. Retrieved from: https://is.cuni.cz/webapps/zzp/download/120298765/?lang=cs

[63] PETŘÍČEK, V., M. DUŠEK and L. PALATINUS. Crystallographic Computing System JANA2006: General features. *Zeitschrift für Kristallographie - Crystalline Materials*. 2014, vol. 229. 10.1515/zkri-2014-1737

[64] Vickers Hardness Test. *Gordon england*. Summer 2019. Retrieved from: http://www.gordonengland.co.uk/hardness/vickers.htm

[65] KOZLÍK, J., P. HARCUBA, J. STRÁSKÝ, H. BECKER, J. ŠMILAUEROVÁ and M. JANEČEK. Microstructure and texture formation in commercially pure titanium prepared by cryogenic milling and spark plasma sintering. *Materials Characterization*. 2019, vol. 151, pp. 1–5. 10.1016/j.matchar.2019.02.035

[66] VÁCLAVOVÁ, K., J. STRÁSKÝ, P. ZHÁŇAL, J. VESELÝ, V. POLYAKOVA, I. SEMENOVA and M. JANEČEK. Ultra-fine grained microstructure of metastable beta Ti-15Mo alloy and its effects on the phase transformations. *IOP Conference Series: Materials Science and Engineering*. 2017, vol. 194, no. 1, p. 012021. 10.1088/1757-899X/194/1/012021

[67] ANSELMI-TAMBURINI, U., S. GENNARI, J.E. GARAY and Z.A. MUNIR. Fundamental investigations on the spark plasma sintering/synthesis process: II. Modeling of current and temperature distributions. *Materials Science and Engineering: A*. 2005, vol. 394, no. 1, pp. 139–148. 10.1016/j.msea.2004.11.019

[68] KOZLÍK, J. *Diploma thesis: Microstructure and texture of titanium prepared by powder metallurgy*. B.m.: Charles University, 2018.

[69] ŠMILAUEROVÁ, J., M. JANEČEK, P. HARCUBA, J. STRÁSKÝ, J. VESELÝ, R. KUŽEL and H.J. RACK. Ageing response of sub-transus heat treated Ti–6.8Mo–4.5Fe–1.5Al alloy. *Journal of Alloys and Compounds*. 2017, vol. 724, pp. 373–380. 10.1016/j.jallcom.2017.07.036

[70] SYARIF, J., T.N. ROHMANNUDIN, M.Z. OMAR, Z. SAJURI and S. HARJANTO. Stability of the beta phase in Ti-Mo-Cr alloy fabricated by powder metallurgy. *Journal of Mining and Metallurgy, Section B: Metallurgy*. 2013, vol. 49, no. 3, pp. 285–292.

[71] GUO, Z., S. MALINOV and W. SHA. Modelling beta transus temperature of titanium alloys using artificial neural network. *Computational Materials Science*. 2005, vol. 32, no. 1, pp. 1–12. 10.1016/j.commatsci.2004.05.004

[72] TERYNKOVÁ, A. *Bakalářská práce: Mikrostruktura a mechanické vlastnosti slitiny Ti15Mo připravené metodou ECAP*. B.m.: Univerzita Karlova, 2017.

[73] XU, W., D.P. EDWARDS, X. WU, M. STOICA, M. CALIN, U. KÜHN, J. ECKERT and K. XIA. Promoting nano/ultrafine-duplex structure via accelerated α precipitation in a β-type titanium alloy severely deformed by high-pressure torsion. *Scripta Materialia*. 2013, vol. 68, no. 1, Architectured Materials, pp. 67–70. 10.1016/j.scriptamat.2012.09.023

[74] BARTA, K. *Disertation: Phase transformations in ultra-fine grained titanium alloys*. B.m.: Universita Karlova, 2019.

[75] XU, W., X. WU, M. STOICA, M. CALIN, U. KÜHN, J. ECKERT and K. XIA. On the formation of an ultrafine-duplex structure facilitated by severe shear deformation in a Ti–20Mo β-type titanium alloy. *Acta Materialia*. 2012, vol. 60, no. 13, pp. 5067–5078. 10.1016/j.actamat.2012.05.042

[76] ŠMILAUEROVÁ, J., P. HARCUBA, D. KRIEGNER, M. JANEČEK and V. HOLÝ. Growth kinetics of ω particles in β-Ti matrix studied by in situ small-angle X-ray scattering. *Acta Materialia*. 2015, vol. 100, pp. 126–134. 10.1016/j.actamat.2015.08.014

[77] KOZLÍK, J., H. BECKER, P. HARCUBA, J. STRÁSKÝ and M. JANEČEK. Cryomilled and spark plasma sintered titanium: the evolution of microstructure. *IOP Conference Series: Materials Science and Engineering*. 2017, vol. 194, p. 012023. 10.1088/1757-899X/194/1/012023

List of Tables

Table 1.1: Typical properties of metastable β-titanium Ti-15Mo alloy……...9

Table 4.1: Default Composition of Ti-15Mo rods as specified by Carpenter Co.....19

Table 4.2: An overview of used sintering conditions and respective labels of samples for both initial and milled powder.....20

Table 5.1: Contamination of initial and milled powder by oxygen, hydrogen and nitrogen in weight percent.....35

Table 5.2: Chemical contamination of chosen samples.....51

List of Abbreviations

AM	Additive manufacturing
ARB	Accumulative roll bonding
BCC	Body-centred cubic
BSE	Back-scattered electrons
CGHE	Carrier gas hot extraction
EBSD	Electron back-scattered diffraction
ECAP	Equal-channel angular pressing
EDX	Energy dispersive X-ray spectroscopy
FEG	Field emission gun
FIB	Focused ion beam
GIS	Gas injection system
HAGB	High angle grain boundary
HCP	Hexagonal close packed
HPT	High pressure torsion
IPF	Inverse pole figure
LAGB	Low angle grain boundary
PM	Powder metallurgy
QIP	Quasi isostatic forging
SA	Stearic acid
SEM	Scanning electron microscopy
SPD	Severe plastic deformation
SPS	Spark plasma sintering
tEBSD	Transmission EBSD
TEM	Transmission electron microscopy
TKD	Transmission Kikuchi diffraction
XRD	X-ray diffraction